Heterogeneous Deformation and Spall of an Extruded Tungsten Alloy: Plate Impact Experiments and Crystal Plasticity Modeling

by T. J. Vogler and J. D. Clayton

ARL-RP-206 **April 2008**

A reprint from the *Journal of the Mechanics and Physics of Solids*, vol. 56, pp. 297–335, 2008.

Approved for public release; distribution is unlimited.

NOTICES

Disclaimers

The findings in this report are not to be construed as an official Department of the Army position unless so designated by other authorized documents.

Citation of manufacturer's or trade names does not constitute an official endorsement or approval of the use thereof.

Destroy this report when it is no longer needed. Do not return it to the originator.

Army Research Laboratory
Aberdeen Proving Ground, MD 21005-5069

ARL-RP-206 **April 2008**

Heterogeneous Deformation and Spall of an Extruded Tungsten Alloy: Plate Impact Experiments and Crystal Plasticity Modeling

T. J. Vogler
Sandia National Laboratories

J. D. Clayton
Weapons and Materials Research Directorate, ARL

A reprint from the *Journal of the Mechanics and Physics of Solids*,
vol. 56, pp. 297–335, 2008.

Approved for public release; distribution is unlimited.

REPORT DOCUMENTATION PAGE

Form Approved
OMB No. 0704-0188

Public reporting burden for this collection of information is estimated to average 1 hour per response, including the time for reviewing instructions, searching existing data sources, gathering and maintaining the data needed, and completing and reviewing the collection information. Send comments regarding this burden estimate or any other aspect of this collection of information, including suggestions for reducing the burden, to Department of Defense, Washington Headquarters Services, Directorate for Information Operations and Reports (0704-0188), 1215 Jefferson Davis Highway, Suite 1204, Arlington, VA 22202-4302. Respondents should be aware that notwithstanding any other provision of law, no person shall be subject to any penalty for failing to comply with a collection of information if it does not display a currently valid OMB control number.

PLEASE DO NOT RETURN YOUR FORM TO THE ABOVE ADDRESS.

1. REPORT DATE *(DD-MM-YYYY)*
April 2008

2. REPORT TYPE
Reprint

3. DATES COVERED (From - To)
October 2005–October 2007

4. TITLE AND SUBTITLE
Heterogeneous Deformation and Spall of an Extruded Tungsten Alloy: Plate Impact Experiments and Crystal Plasticity Modeling

5a. CONTRACT NUMBER

5b. GRANT NUMBER

5c. PROGRAM ELEMENT NUMBER

6. AUTHOR(S)
T. J. Vogler* and J. D. Clayton

5d. PROJECT NUMBER
WHPR01B

5e. TASK NUMBER

5f. WORK UNIT NUMBER

7. PERFORMING ORGANIZATION NAME(S) AND ADDRESS(ES)
U.S. Army Research Laboratory
ATTN: AMSRD-ARL-WM-TD
Aberdeen Proving Ground, MD 21005-5069

8. PERFORMING ORGANIZATION REPORT NUMBER
ARL-RP-206

9. SPONSORING/MONITORING AGENCY NAME(S) AND ADDRESS(ES)

10. SPONSOR/MONITOR'S ACRONYM(S)

11. SPONSOR/MONITOR'S REPORT NUMBER(S)

12. DISTRIBUTION/AVAILABILITY STATEMENT
Approved for public release; distribution is unlimited.

13. SUPPLEMENTARY NOTES
A reprint from the *Journal of the Mechanics and Physics of Solids*, vol. 56, pp. 297–335, 2008.
*Sandia National Laboratories, Albuquerque, NM 87185-1181

14. ABSTRACT

The role of microstructure in the dynamic deformation and fracture of a dual phase, polycrystalline tungsten alloy under high-rate impact loading is investigated via experiments and modeling. The material studied consists of pure tungsten crystals embedded in a ductile binder alloy comprised of tungsten, nickel, and iron. The tungsten crystals are elongated in a preferred direction of extrusion during processing. Plate impact tests were conducted on samples oriented either perpendicular or parallel to the extrusion direction. Spatially resolved interferometric data from these tests were used to extract wave propagation behavior and spall strength dependent upon position in the sample microstructure. Finite element simulations of impact and spall in digitally reproduced microstructural geometries were conducted in parallel with the experiments. Finite deformation crystal plasticity theory describes the behavior of the pure tungsten and binder phases, and a stress- and temperature-based cohesive zone model captures fracture at grain and phase boundaries in the microstructure. In results from both experiments and modeling, the grain orientations affect the free-surface velocity profile and spall behavior. Some aspects of distributions of free-surface velocity and spall strength among different microstructure configurations are qualitatively similar between experimental and numerical results, while others are not as a result of differing scales of resolution and modeling assumptions. Following a comparison of experimental and numerical results for different microstructures, intergranular fracture is identified as an important mechanism underlying the spall event.

15. SUBJECT TERMS
microstructures, tungsten, crystal plasticity, fracture, spall, plate impact, finite elements, probability and statistics

16. SECURITY CLASSIFICATION OF:

a. REPORT	**b. ABSTRACT**	**c. THIS PAGE**	**17. LIMITATION OF ABSTRACT**	**18. NUMBER OF PAGES**
UNCLASSIFIED	UNCLASSIFIED	UNCLASSIFIED	UL	46

19a. NAME OF RESPONSIBLE PERSON
J. D. Clayton

19b. TELEPHONE NUMBER (*Include area code*)
410-278-6146

Available online at www.sciencedirect.com

ScienceDirect

Journal of the Mechanics and Physics of Solids 56 (2008) 297–335

JOURNAL OF THE MECHANICS AND PHYSICS OF SOLIDS

www.elsevier.com/locate/jmps

Heterogeneous deformation and spall of an extruded tungsten alloy: plate impact experiments and crystal plasticity modeling

T.J. Vogler[a,*], J.D. Clayton[b]

[a]*Solid Dynamics and Energetic Materials Department, Sandia National Laboratories, Albuquerque, NM 87185-1181, USA*
[b]*Impact Physics Branch, US Army Research Laboratory, Aberdeen Proving Ground, MD 21005-5069, USA*

Received 5 February 2007; received in revised form 1 June 2007; accepted 4 June 2007

Abstract

The role of microstructure in the dynamic deformation and fracture of a dual phase, polycrystalline tungsten alloy under high-rate impact loading is investigated via experiments and modeling. The material studied consists of pure tungsten crystals embedded in a ductile binder alloy comprised of tungsten, nickel, and iron. The tungsten crystals are elongated in a preferred direction of extrusion during processing. Plate impact tests were conducted on samples oriented either perpendicular or parallel to the extrusion direction. Spatially resolved interferometric data from these tests were used to extract wave propagation behavior and spall strength dependent upon position in the sample microstructure. Finite element simulations of impact and spall in digitally reproduced microstructural geometries were conducted in parallel with the experiments. Finite deformation crystal plasticity theory describes the behavior of the pure tungsten and binder phases, and a stress- and temperature-based cohesive zone model captures fracture at grain and phase boundaries in the microstructure. In results from both experiments and modeling, the grain orientations affect the free-surface velocity profile and spall behavior. Some aspects of distributions of free-surface velocity and spall strength among different microstructure configurations are qualitatively similar between experimental and numerical results, while others are not as a result of differing scales of resolution and modeling assumptions. Following a comparison of experimental and numerical results for different microstructures, intergranular fracture is identified as an important mechanism underlying the spall event.

© 2007 Elsevier Ltd. All rights reserved.

Keywords: Microstructures; Crystal plasticity; Plate impact; Finite elements; Probability and statistics

---

1. Introduction

The response of solid materials to impact or shock loading conditions is of interest for a variety of applications, including structural crashworthiness, ballistic events, and explosive–structure interactions. Often such materials are heterogeneous when considered at the microscale; examples include polycrystalline metals and ceramics or composite systems. Here we use the terms microscale and mesoscale somewhat interchangeably, as both are encountered in the literature to describe the physics and mechanics of

---

[*] Corresponding author. Tel.: +1 505 845 0742; fax: +1 505 845 7685.
E-mail address: tjvogle@sandia.gov (T.J. Vogler).

0022-5096/$ - see front matter © 2007 Elsevier Ltd. All rights reserved.
doi:10.1016/j.jmps.2007.06.013

deformation at the scale of material features such as individual grains or particles, which can occur over 10^{-7}–10^{-2} m. For most metals and ceramics, the mesoscale is identified with the grain size, typically on the order of 10^{-6}–10^{-4} m. The microstructure has been experimentally observed to affect shock wave propagation and material failure in various solids in a number of instances (cf. Asay and Barker, 1974; Asay and Chhabildas, 2003; Brannon et al., 1983; Mescheryakov, 2003). Even so, the mesoscale remains difficult to probe experimentally in shock experiments due to the short time scales involved for stress waves to traverse individual grains. Early modeling efforts (e.g., Meyers and Carvalho, 1976) pointed toward heterogeneous shock propagation phenomena controlled by the mesoscale, but only recently has it been possible to computationally address realistic microstructures, with dimensions of several hundred microns, with advanced crystal mechanics-based constitutive models for nonlinear elastic–plastic behavior at the grain scale.

1.1. Background: experimental methods

Velocity interferometry has long been an important tool in shock physics research with the velocity interferometer system for any reflector (VISAR) (Barker, 2000) system and Fabry–Perot (McMillan et al., 1988) velocimeter being the most widely used. Bloomquist and Sheffield (1983) developed the optically recording velocity interferometer system (ORVIS) in which the photodetectors of a VISAR system are replaced by a streak camera. Their objective, though, was improved temporal resolution, and they did not consider spatially resolved phenomena. Baumung et al. (1996) made improvements to the system to allow use of a more modest laser and to allow many measurements across the width of the line. The current system, which we will refer to as the line-VISAR, is an improved version of that of Baumung et al. and is described in Trott et al. (2001). Additional references relating to efforts towards spatially resolved velocity measurements in dynamic experiments can also be found therein. The length of the line imaged by the system can be varied from less than a millimeter to tens of millimeters by changing the optics. The line-VISAR represents a significant advance over other diagnostics because it can be used to study spatially varying phenomena, whether they arise due to multidimensional effects or material heterogeneity.

The line-VISAR has been utilized in the study of a variety of physical phenomena at the mesoscale for a number of different classes of materials. Phenomena studied include: dynamic loading of well-ordered systems such as lattices of tin spheres (Baer and Trott, 2004) and preformed ceramic lattices (Trott et al., 2007b); yielding, spall, and void growth in tantalum (Chhabildas et al., 2002; Furnish et al., 2006); collapse of holes in copper samples (Furnish et al., 2004); and compaction of granular sugar (Furnish et al., 2006). The line-VISAR has also been used to probe the shock response of materials such as fused silica, foam, glass-reinforced polyester (Trott et al., 2000), boron carbide (Vogler et al., 2004), and HMX (Baer and Trott, 2005).

Although the line-VISAR has been used as a diagnostic for several different types of experiments, in general it has been used to assess phenomena qualitatively rather than quantitatively. However, in a few instances line-VISAR data have been analyzed directly to determine void growth (Chhabildas et al., 2002) and spatial variability of the Hugoniot elastic limit (HEL) and spall strength (Furnish et al., 2006).

1.2. Background: modeling techniques

Crystal plasticity models capturing anisotropy arising from individual slip system activity have been used to describe deformation of metallic materials for some time (see, e.g., Asaro, 1983; Kocks et al., 1998). Historically, most crystal plasticity implementations have focused on the quasi-static loading regime, though models have been applied in the intermediate strain rate regime to address dynamic phenomena such as those occurring in Hopkinson bar experiments (Nemat-Nasser et al., 1998), Taylor impact experiments (Schoenfeld, 1998), explosive forming of polycrystalline tantalum liners (Schoenfeld, 1998), and ballistic impact of titanium armor plates (Schoenfeld and Kad, 2002).

Recently, the crystal plasticity approach with resolution of individual grains by many finite elements has been applied to model the very high-rate (shock) loading regime (Becker, 2004; Clayton, 2005b). Simulations in this regime are often more computationally intensive than for quasi-static loading because the former require large domains due to the lack of a representative volume element (RVE) in the direction of shock propagation and the refined meshes needed to resolve stress waves, shock fronts, and material instabilities.

Small time steps are also necessary to capture details of the shock wave processes, irrespective of the choice of numerical integration scheme. In particular, Becker's (2004) simulations of polycrystalline tantalum demonstrated heterogeneities of stress and deformation at the grain scale, and shock fronts whose roughness decreased significantly as the applied stress rose from 10 to 100 GPa. Becker also pointed out the presence of non-uniformities in the free-surface velocity that would complicate interferometric velocity measurements in analogous plate impact experiments. It is precisely these variations that are the focus of the current investigation.

Spall fracture and wave propagation in polycrystalline ceramics have been studied numerically with cohesive finite elements addressing fracture at grain boundaries (Espinosa and Zavattieri, 2003a, b). In that particular study, in which the bulk behavior was dictated by isothermal, anisotropic linear elasticity, local fracture behavior and heterogeneous wave propagation were observed. Comprehensive parametric studies with variable cohesive properties and mesh densities were the focus of the investigation, and although the simulations mimicked plate impact tests, direct comparisons with experimental data were not reported.

An alternative to the finite element method (FEM) that has recently been employed to resolve the shock deformation of polycrystalline metals at the mesoscale is the discrete-element method (DEM) (Case and Horie, 2007; Yano and Horie, 1999, 2002). Simulations using this technique have, to date, been 2D and utilized very simple means to account for grain-to-grain variations in behavior, specifically orientation-dependent HELs, elastic wave speeds, and plastic wave speeds. Nonetheless, DEM models have displayed a rich set of physically realistic behaviors including a non-uniform shock front, lateral motion near the shock, and vortices in material motion.

In most of the cases cited above, few comparisons were made between simulation results and experimental data on behavior at the mesoscale, in large part because of a lack of available experimental data in that spatial regime. In a few cases, line-VISAR results have been compared to numerical simulations of the dynamic loading of granular sugar packings (Trott et al., 2007a) and ordered packings of tin spheres (Baer and Trott, 2004). These have been large-scale 3D numerical simulations conducted with Eulerian hydrocodes, as opposed to Lagrangian FEM or DEM. Furthermore, these simulations have focused on the effects engendered by variations in spatial distributions of spherical or cubic particles in regular or random arrays, in the context of relatively simple isotropic elastic or elastic–plastic constitutive theories for the deviatoric response. In these instances, comparison between the simulations and experimental results have generally focused on comparing the average response or homogenized material properties.

1.3. Background: tungsten alloys

Tungsten heavy alloys (WHA) such as the one studied here have been studied extensively, primarily as potential materials for kinetic energy (KE) projectiles (Magness, 1994). Mechanical properties and physical phenomena at high strain rates have been obtained or observed using Hopkinson bar techniques (Ramesh and Coates, 1992; Weerasooriya and Beaulieu, 1993), normal plate impact (Bless and Chau, 2006; Dandekar and Weisgerber, 1999; Millett et al., 1999; Zurek and Gray, 1991), explosive loading (Baoping et al., 1994), and oblique flyer-plate impact (Zhou and Clifton, 1997). In most of these, the bulk mechanical properties of the homogenized multiphase material (e.g., stress–strain curves, Hugoniot data, and spall strengths) were of primary interest, though some effects of local behavior dominated by microstructure, such as fracture surfaces or shear localization initiation sites, have been reported and described.

The role of microstructure on dynamic mechanical properties of tungsten alloys has also been investigated via constitutive modeling and numerical simulation. Zhou and co-workers used an isotropic elastic-viscoplastic constitutive model with realistic grain structures to capture shear localization in oblique impact (pressure–shear conditions) (Zhou et al., 1994) and high-rate nominally uniform shear deformation (Zhou, 1998). Effective properties of tungsten alloys depending on microstructural parameters (e.g., volume fraction, size, and distribution of pure tungsten grains) were also determined numerically (Love and Batra, 2005).

The above modeling studies incorporated isotropic constitutive models for pure tungsten, a body-centered cubic (BCC) material whose single crystals are virtually elastically isotropic at low pressures (Hirth and Lothe, 1982) yet are known to exhibit significant anisotropy with regards to plastic flow (Argon and Maloof, 1966; Subhash et al., 1994). To address the effects of crystallographic orientation and dislocation accumulation on the thermomechanical response of tungsten alloys, crystal plasticity-based constitutive models have recently been formulated and implemented by one of the authors. Tensile deformation and fracture of realistically rendered (Clayton, 2005a) and homogenized (Clayton, 2006a) microstructures of dual phase tungsten alloys have been studied, respectively, with cohesive zone and anisotropic continuum damage mechanics theories. Clayton (2005b) performed 2D simulations of high-rate, uniaxial strain compression and spall fracture of a two-phase tungsten heavy alloy. It was found that grain shapes and orientations had a significant effect on the nature of propagating stress waves, while spall was influenced by both of these aspects as well as by the local interfacial properties used in the model. Statistical variations of free-surface velocity were also found to vary with crystal orientation, texture, and temperature dependence of properties controlling grain boundary fracture (Clayton, 2006b).

1.4. *Objectives and scope*

In this paper, new results are presented for planar impact experiments on WHA in conjunction with new results from simulations obtained using the crystal plasticity-cohesive fracture modeling methods developed by Clayton (2005b). The line-VISAR utilized in the experiments provides spatially- and temporally resolved data on material deformation. It also provides statistical information regarding the local spall strength of the material. Aspects of the material response not reported in previous modeling of impact (Clayton, 2005b, 2006b) are studied through experiments and simulations here, including different impact velocities and variations in orientations of extruded grain structures (i.e., elongated grains oriented perpendicular or parallel to the compression wave).

Although comparison between experiments and simulations is not straightforward at present due to competing limitations on the spatial resolution of the experimental system and the absolute size of the computational domain, it is possible to compare trends observed in experimental results with those from the simulations such as the effect of microstructural orientation on average spall strength. Changes in free-surface velocities and corresponding statistics of the response with increasing impact velocity or changes in sample orientation can be compared between model and experiment. For example, changes in variance of free-surface velocity with changes in grain orientation may or may not be reflected by either the experiments or the simulations. Furthermore, the capability for the simulations to detect features of the experimental results, such as characteristic spikes in velocity dispersion through the shock front (cf. Case and Horie, 2007), provides an important means to assess the validity of the simulations. In this way, experiments enable validation and possible improvement of crystal elasticity and plasticity models for high-rate applications, and simulations offer explanations and insight into macroscopic and mesoscopic aspects of material behavior—either observed or predicted—that are difficult to resolve or deduce through experiments alone. This work represents a crucial first step toward developing meaningful ways to compare the two sets of results.

Cartesian coordinates are used, with summation implied over repeated indices. Vector and tensor quantities are represented with boldface type, while scalars and individual components of vectors and tensors are written in italics. Juxtaposition implies summation over two repeated adjacent indices (e.g., $(\mathbf{AB})_a^{\ b} = A_{ac}B^{cb}$). The dot (scalar) product of vectors is represented by the symbol "•" (e.g., $\mathbf{a}\bullet\mathbf{b} = a^a b_a$). The colon denotes contraction over repeated pairs of indices (e.g., $\mathbf{A}:\mathbf{B} = \mathrm{tr}\left(\mathbf{A}^{\mathrm{T}}\mathbf{B}\right) = A_{ab}B^{ab}$ and $\mathbf{C}:\mathbf{A} = C^{abcd}A_{cd}$). The symbol "$\otimes$" represents the tensor (outer) product (e.g., $(\mathbf{a}\otimes\mathbf{b})^{ab} = a^a b^b$). Superposed -1, T, and "•" denote inverse, transpose, and material time derivative operations, respectively. Additional notation is explained as it appears.

2. Experimental approach

2.1. *Material*

The tungsten alloy studied consists of grains of relatively brittle pure tungsten (BCC) in a relatively soft and ductile face-centered cubic (FCC) matrix composed of nickel (50% by weight), iron (25%), and tungsten (25%). The alloy nominally consists of 90% tungsten grains and 10% matrix alloy, yielding an overall mass composition of 93W–5Ni–2Fe. The composite is fabricated through isostatic pressing and sintering of a mixture of W, Ni, and Fe powders. The alloy is then annealed to remove absorbed hydrogen and may be quenched, swaged, or pre-twisted to enhance its dynamic properties. Typical grain sizes are 10–30 μm for the W crystals and 200–500 μm for the matrix phase, implying that each matrix grain contains several W grains. The average density of the material was found to be $17.77 \pm 0.07\,\mathrm{g/cm^3}$.

As a result of the swaging process, the W grains are elongated in the direction of the axis of the KE rod from which material was obtained. As a means to assess the effect of the microstructure on shock wave propagation and spall failure, thin plates with two orientations were tested. The first, shown as a disk Fig. 1(a) and referred

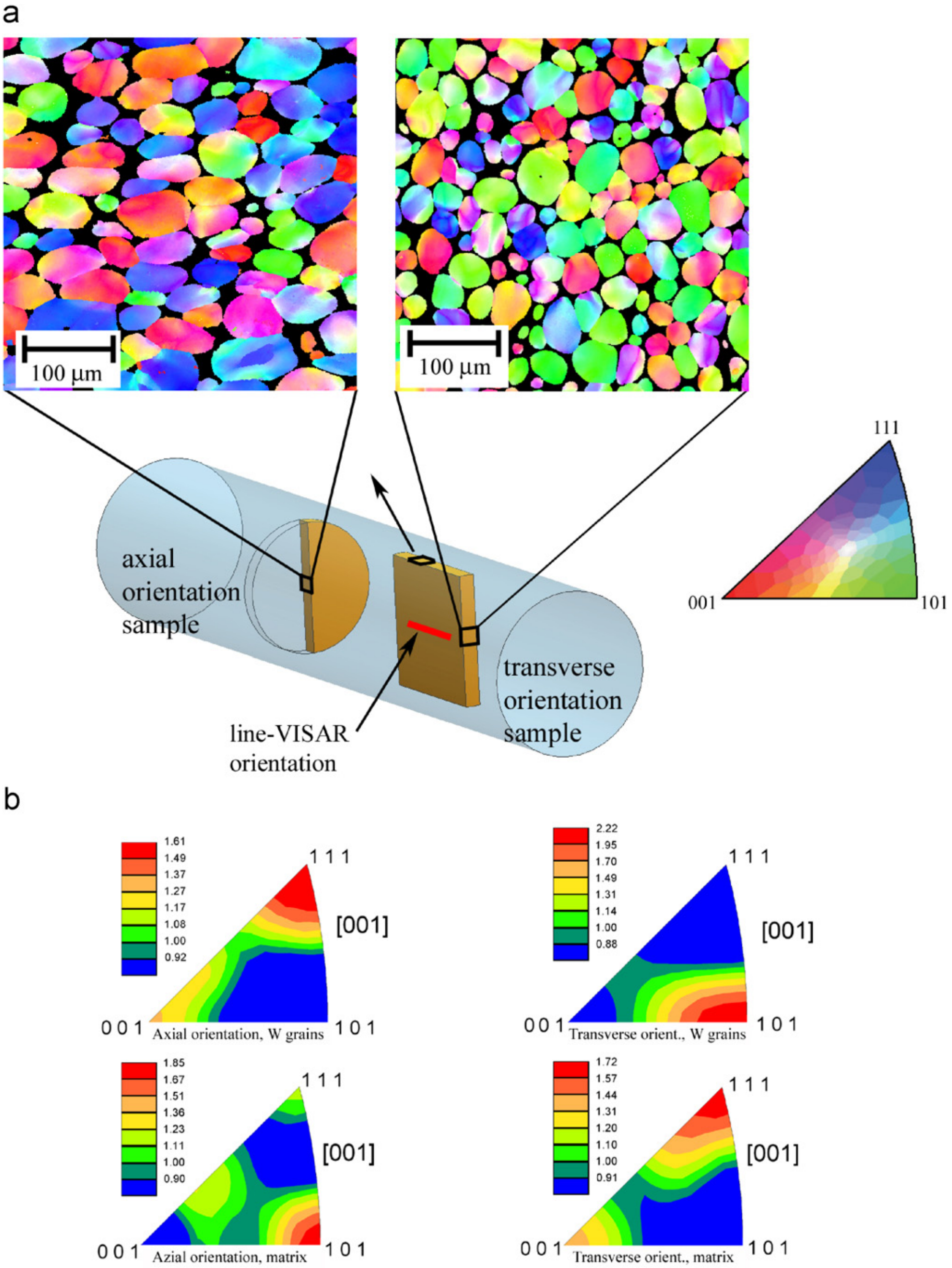
a
100 μm
100 μm
axial orientation sample
transverse orientation sample
line-VISAR orientation
111
001
101
b
1.61
1.49
1.37
1.27
1.17
1.08
1.00
0.92
1 1 1
[001]
0 0 1
1 0 1
Axial orientation, W grains
2.22
1.95
1.70
1.49
1.31
1.14
1.00
0.88
1 1 1
[001]
0 0 1
1 0 1
Transverse orient., W grains
1.85
1.67
1.51
1.36
1.23
1.11
1.00
0.90
1 1 1
[001]
0 0 1
1 0 1
Azial orientation, matrix
1.72
1.57
1.44
1.31
1.20
1.10
1.00
0.91
1 1 1
[001]
0 0 1
1 0 1
Transverse orient., matrix

Fig. 1. (a) Schematic of sample orientations relative to penetrator axis and anisotropic WHA microstructure. W grains colored by lattice orientation from EBSD scans; (b) Inverse pole figures for W grains and matrix material for the two sample orientations.

to as the axial orientation, aligns the sample normal with the axis of the rod, giving elongated W grains through the sample thickness as shown in the electron backscatter diffraction (EBSD) image in the upper left. The second, shown as a thin square sample in Fig. 1(a) and referred to as the transverse orientation, has a sample normal that is perpendicular to the axis of the rod. For these samples, two edges show equiaxed grains as shown in the upper right EBSD image, while the other two edges and the sample faces reveal the elongated grains of the upper left EBSD image. The line-VISAR was thus oriented with respect to the grains as illustrated in Fig. 1(a) in order to account for in-plane anisotropy of the sample. Inverse pole figures of the W grains (BCC) and binder phase (FCC) are shown in Fig. 1(b), with the distribution of crystallographic directions plotted with respect to the specimen normal, denoted by [0 0 1], of the image for each orientation shown in Fig. 1(a). The relatively mild textures are indicative of axial extension, drawing, or extrusion operations (Kocks et al., 1998): a preference for $\langle 1\,1\,0 \rangle$ (i.e., $\langle 1\,0\,1 \rangle$) orientations for the BCC grains in the transverse microstructure, and a preference for $\langle 1\,1\,1 \rangle$ and $\langle 1\,0\,0 \rangle$ orientations for the FCC grains in the transverse microstructure. Despite the orientation dependence of the composite microstructure, the homogenized material is essentially elastically isotropic at the macroscale with longitudinal and shear wave speeds of 5.19 and 2.83 km/s, respectively. Note that pure tungsten is an unusual cubic material in that its single crystals are elastically isotropic at low pressures (Hirth and Lothe, 1982), though deviations from elastic isotropy and phase transformations occur at very high pressures (Ruoff et al., 1998). Hence, any deviations from elastic isotropy in the WHA are caused by finite deformations or the presence and distribution of the presumably anisotropic binder phase, as well as local lattice imperfections such as grain, twin, or subgrain boundaries.

2.2. Plate impact experiments

Five plate impact experiments were performed. A compressed gas gun was used to launch a 1.5 mm thick WHA impactor into a 3.0 mm thick WHA target at velocities of approximately 250, 350, and 450 m/s. Two samples were in the axial orientation and the other three were transversely oriented. All impactors had axial orientation. Details for the five experiments are given in Table 1, and a schematic of the experimental set-up is shown in Fig. 2. The WHA impactor was mounted on a TPX (polymethylpentene) layer to give a nearly complete unloading, and that in turn was mounted on the front of an aluminum projectile. Projectile velocities were measured to better than 0.5% by means of three shorting pins of different heights, and tilts were determined through four pins distributed around the circumference of the sample. In all cases except experiment WHA-5 the tilt was less than 0.5 mrad. In experiment WHA-5, it appeared that there was separation of the WHA impactor from the projectile sometime prior to impact since the tilt pins indicated only a small tilt but the line-VISAR streaks indicated significant tilt; also, the impactor may not have been entirely planar, perhaps due to bowing. The back surface of the target was diamond turned and then diffused with glass beads to facilitate good reflectance for the line-VISAR system used to monitor the velocity. Following the experiment, debris was collected for metallographic analysis, which will be reported separately in the future. It should be noted that no special precautions were taken to ensure “soft” recovery of the sample since it will inevitably strike the reflecting mirror of the line-VISAR.

Table 1
Details of plate impact experiments

Expt.	Sample orient.	Impactor/target thickness (mm)	V_I (km/s)	HEL (GPa)	U_s^p (km/s)	σ_h (GPa)	ρ_h (g/cm^3)
WHA-1	Axial	1.54/3.07	0.249	2.54	4.20	−9.63	18.27
WHA-2	Axial	1.54/3.06	0.345	2.40	4.27	−13.35	18.48
WHA-3	Transverse	1.47/2.96	0.246	0.83	4.20	−9.31	18.30
WHA-4	Transverse	1.48/2.95	0.347	4.09	4.10	−13.16	18.53
WHA-5	Transverse	1.48/2.95	0.426	2.86	4.06	−15.81	18.73

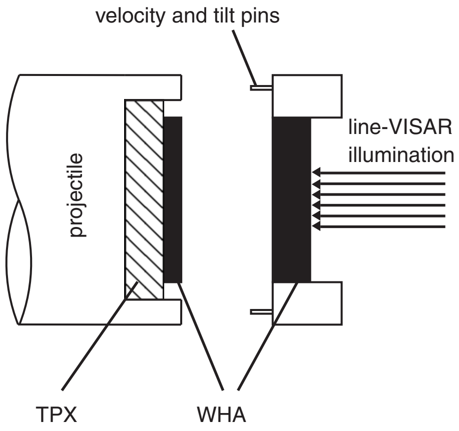

Fig. 2. Set-up for plate impact experiments.

3. Modeling approach

Essential features of the constitutive models for tungsten and binder phases are given here, followed by a brief description of the cohesive fracture model used for describing failure along internal material interfaces. Descriptions of the numerical simulations are then provided. The reader is referred to Clayton (2005a, b) for further details, including values of parameters.

3.1. Crystal plasticity theory

A finite deformation, rate-dependent crystal plasticity model is used to capture the thermomechanical behavior of the tungsten crystals and W–Ni–Fe binder phase. The same model framework, albeit with different parameters, is used for each material.

Denoted by $\mathbf{x} = \mathbf{x}(\mathbf{X}, t)$ is a smooth time-dependent motion, where $\mathbf{x}$ and $\mathbf{X}$ are spatial and reference coordinates, respectively. The local deformation gradient $\mathbf{f}$ is decomposed as

$$\mathbf{f} \equiv \frac{\partial \mathbf{x}}{\partial \mathbf{X}} = \mathbf{f}^{\mathbf{e}}\mathbf{f}^{\boldsymbol{\theta}}\mathbf{f}^{\mathbf{p}}, \tag{1}$$

where $\mathbf{f}^{\mathbf{e}}$, $\mathbf{f}^{\boldsymbol{\theta}}$, and $\mathbf{f}^{\mathbf{p}}$ denote the kinematics of elasticity and rigid-body rotation, stress-free thermal expansion or contraction, and the cumulative contribution of moving crystal defects. The plastic velocity gradient in the intermediate configuration is defined as

$$\bar{\mathbf{l}}^{\mathbf{p}} \equiv \dot{\mathbf{f}}^{\mathbf{p}}\mathbf{f}^{\mathbf{p}-1} = \sum_{\alpha=1}^{n} \dot{\gamma}^{(\alpha)}\mathbf{s}_0^{(\alpha)} \otimes \mathbf{m}_0^{(\alpha)}, \tag{2}$$

with $\dot{\gamma}^{(\alpha)}$ the shearing rate on slip system α, and n the number of potentially active slip systems, each with slip direction $\mathbf{s}$ and slip plane normal $\mathbf{m}$.

Local balance laws in the spatial configuration are

$$\dot{\rho} + \rho\,\mathrm{tr}(\mathbf{l}) = 0, \quad \mathrm{div}\,\boldsymbol{\sigma} + \rho\mathbf{b} = \rho\ddot{x}, \quad \boldsymbol{\sigma} = \boldsymbol{\sigma}^{\mathrm{T}}, \quad \rho\dot{e} + \mathrm{div}\,\mathbf{q} = \mathrm{tr}(\boldsymbol{\sigma}\mathbf{l}), \tag{3}$$

with ρ, $\mathbf{l}$, $\boldsymbol{\sigma}$, $\mathbf{b}$, e, and $\mathbf{q}$ denoting the current mass density, spatial velocity gradient, Cauchy stress tensor, body force vector per unit mass, internal energy per unit mass, and heat flux vector per unit current area, respectively. The local entropy inequality is written as

$$\rho\dot{\eta} \geqslant -\,\mathrm{div}\left(\mathbf{q}/\theta\right), \tag{4}$$

with $\dot{\eta}$ the time rate of entropy production per unit mass, θ the absolute temperature, and div the spatial divergence. The Helmholtz free energy per unit mass is of the functional form

$$\psi = \psi(\mathbf{e}^{\mathrm{e}}, \theta, \xi), \tag{5}$$

where the intermediate configuration elastic strain $2\mathbf{e}^{\mathrm{e}} = \mathbf{f}^{\mathrm{e}\mathrm{T}}\mathbf{f}^{\mathrm{e}} - \mathbf{1}$. The symbol ξ denotes a dimensionless scalar internal variable representing stored micro-elastic energy associated with crystal defects. From Eqs. (2)–(5), one may deduce the following constitutive relationships:

$$\mathbf{s}^{\mathrm{e}} = \tilde{\rho}\partial_{\mathbf{e}^{\mathrm{e}}}\psi, \tag{6}$$

$$\eta = \alpha_{\mathrm{T}}\mathrm{tr}(\boldsymbol{\sigma})/\rho - \partial_\theta\psi, \tag{7}$$

$$\sum_{\alpha=1}^{n}\tau^{(\alpha)}\dot{\gamma}^{(\alpha)} - \rho\left(\partial_\xi\psi\right)\dot{\xi} \geqslant \frac{\mathbf{q}\bullet\nabla_{\mathbf{x}}\theta}{\theta}, \tag{8}$$

where α_{T} is the coefficient of isotropic thermal expansion, the elastic second Piola–Kirchhoff stress $(s^{\mathrm{e}})^{\alpha\beta} \equiv j^{\mathrm{e}} f^{\mathrm{e}-1\alpha}_{a}\sigma^{ab} f^{\mathrm{e}-1\beta}_{b}$ with $j^{\mathrm{e}} \equiv \tilde{\rho}/\rho = \det\mathbf{f}^{\mathrm{e}}$, and the resolved shear stress $\tau^{(\alpha)} \equiv \boldsymbol{\sigma} : (\mathbf{s}^{(\alpha)} \otimes \mathbf{m}^{(\alpha)})$. The spatial gradient is written as ∇_{x}. Isotropic heat conduction in the spatial frame is dictated by Fourier's law:

$$\mathbf{q} = -k\nabla_{\mathbf{x}}\theta, \tag{9}$$

with $k(\mathbf{x}, \theta)$ the spatial thermal conductivity. Defining the specific heat capacity $\hat{c} \equiv \partial_\theta e$, the local energy balance can be written as

$$\underbrace{\rho\hat{c}\dot{\theta}}_{\text{temperature change}} = \underbrace{\sum_{\alpha=1}^{n}\tau^{(\alpha)}\dot{\gamma}^{(\alpha)}}_{\text{plastic dissipation}} \underbrace{-\rho\left(\left(\partial_\xi\psi\right) - \theta\left(\partial_{\theta\xi}\psi\right)\right)\dot{\xi}}_{\text{energy of lattice defects}} + \underbrace{\rho\theta\partial_{\theta\mathbf{e}^{\mathrm{e}}}\psi : \dot{\mathbf{e}}^{\mathrm{e}}}_{\text{thermoelastic coupling}} + \underbrace{\mathrm{div}(k\nabla_{\mathbf{x}}\theta)}_{\text{heat conduction}}. \tag{10}$$

The subsequent discussion pertains specifically to the cubic metallic materials (i.e., phases of tungsten alloy) of interest. A free energy potential per unit intermediate configuration volume is specified as

$$\tilde{\rho}\psi = K_0(\theta)\vartheta^2/2 - K_1\vartheta^3/3 + \mu(\theta)\mathbf{e}^{\mathrm{e}'} : \mathbf{e}^{\mathrm{e}'} + \kappa\mu(\theta)\xi^2/2 + z(\theta), \tag{11}$$

where $\vartheta \equiv \mathrm{tr}(\mathbf{e}^{\mathrm{e}})$ measures the elastic volume change, K_0, K_1, and μ are elastic stiffness coefficients and κ is a dimensionless scalar. The deviatoric elastic strain tensor is defined by $\mathbf{e}^{\mathrm{e}'} \equiv \mathbf{e}^{\mathrm{e}} - \left(\vartheta/3\right)\mathbf{1}$, and $z(\theta)$ accounts for the purely thermal energy.

The time rate of plastic deformation within each phase of the bulk material follows from

$$\dot{\gamma}^{(\alpha)} = \dot{\gamma}_0\left(\tilde{\tau}^{(\alpha)}/g^{(\alpha)}\right)^h \mathrm{sgn}\left(\tilde{\tau}^{(\alpha)}\right). \tag{12}$$

Above, $\dot{\gamma}_0$ and h are material parameters, $g^{(\alpha)}$ is the slip or shearing resistance, $\tilde{\tau}^{(\alpha)} \equiv j^{\mathrm{e}}\tau^{(\alpha)}$, and $\mathrm{sgn}(x) = x/|x|$, with $\mathrm{sgn}(0) = 1$. Thermal softening at high temperatures is incorporated via

$$g^{(\alpha)} = g^{(\alpha)}_0\left(\theta/\theta_0\right)^r, \tag{13}$$

with $g^{(\alpha)}_0$ the flow resistance at reference temperature θ_0 and r a dimensionless constant. The following relationship is assumed between hardening and internal variable $\xi = b\sqrt{\rho_{\mathrm{T}}}$:

$$\frac{1}{n}\sum_{\alpha=1}^{n}\left(g^{(\alpha)}_0 - g^{(\alpha)}_y\right) = \hat{\alpha}\mu(\theta_0)\xi, \tag{14}$$

with $g^{(\alpha)}_y$ an initial yield stress, b the magnitude of the Burgers vector in the reference lattice, and ρ_{T} the total dislocation line length per unit intermediate configuration volume. The scalar $\hat{\alpha}$ accounts for dislocation interactions, while both lattice friction stress and effects of initial dislocation density are incorporated in the initial yield stress $g^{(\alpha)}_y$. Evolution of slip resistance at reference temperature θ_0 is dictated by a hardening-minus-dynamic-recovery relation:

$$\dot{g}_0^{(\alpha)} = A\sum_{\beta=1}^{n} q_\beta^\alpha |\dot{\gamma}^{(\beta)}| - Bg_0^{(\alpha)}\sum_{\beta=1}^{n}|\dot{\gamma}^{(\beta)}|, \quad q_\beta^\alpha = \delta_\beta^\alpha + q(1-\delta_\beta^\alpha), \tag{15}$$

where q is the latent hardening ratio in the interaction matrix q_β^α. Specifically for pure W grains, slip occurs in the $\langle 1\,1\,1\rangle$ directions on any of the $\{1\,1\,0\}$ and $\{1\,1\,2\}$ families of planes, meaning the number of potentially active slip systems is $n = 24$. In the W–Ni–Fe binder phase, the number of potentially active slip systems is $n = 12$. Dislocations are assumed to glide in $\langle 1\,1\,0\rangle$ directions on $\{1\,1\,1\}$ planes for this FCC metal.

3.2. Interfacial fracture model

In the model exercised here, fractures may occur along W–W grain boundaries and W–matrix boundaries in the two-phase alloy. Intragranular cleavage and separation at matrix–matrix grain boundaries are not represented.

Fracture surfaces initiate at interfaces when the traction resolved on the potential initiation site exceeds the intrinsic temperature-dependent strength of the interface:

$$\hat{s} = \hat{s}_0 + \hat{s}_1(\theta - \theta_0), \quad \hat{\tau} = \hat{\tau}_0 + \hat{\tau}_1(\theta - \theta_0), \tag{16}$$

where $\hat{s}$ and $\hat{\tau}$ are the resolved normal traction and shear traction on the interfacial surface, per unit reference area, and $\hat{s}_0$ and $\hat{\tau}_0$ are material parameters. Linearly temperature-dependent initiation strengths—capturing ductile–brittle transitions, for example—are captured by nonzero values of $\hat{s}_1$ and $\hat{\tau}_1$, and mixed-mode initiation criteria are specified by the ratio $\hat{s}_0/\hat{\tau}_0$.

Degraded material at cohesive interfaces, subsequently following fracture initiation, supports local stresses decaying with separation distance as follows:

$$\begin{aligned} \hat{s} &= (\hat{s}_0 + \hat{s}_1(\theta-\theta_0))\left(1-\frac{\delta_\mathrm{n}}{\delta_\mathrm{c}}\right) \quad \text{(loading)},\\ \hat{s} &= (\hat{s}_0 + \hat{s}_1(\theta-\theta_0))\left(1-\frac{\delta_\mathrm{n1}}{\delta_\mathrm{c}}\right)\frac{\delta_\mathrm{n}}{\delta_\mathrm{n1}}, \quad \text{(unloading)}, \end{aligned} \tag{17}$$

$$\begin{aligned} \hat{\tau} &= (\hat{\tau}_0 + \hat{\tau}_1(\theta-\theta_0))\left(1-\frac{|\delta_\mathrm{t}|}{\delta_\mathrm{c}}\right)\left(1-\frac{\langle\delta_\mathrm{n}\rangle}{\delta_\mathrm{c}}\right)\mathrm{sgn}(\delta_\mathrm{t}) \quad \text{(loading)},\\ \hat{\tau} &= (\hat{\tau}_0 + \hat{\tau}_1(\theta-\theta_0))\left(1-\frac{|\delta_\mathrm{t1}|}{\delta_\mathrm{c}}\right)\left(1-\frac{\langle\delta_\mathrm{n}\rangle}{\delta_\mathrm{c}}\right)\frac{\delta_\mathrm{t}}{|\delta_\mathrm{t1}|} \quad \text{(unloading)}, \end{aligned} \tag{18}$$

with δ_n and δ_t the normal and tangential crack openings, δ_n1 and δ_t1 the maximum values of δ_n and δ_t achieved over the deformation history, and δ_c a material parameter describing the separation distance beyond which the cohesive interface no longer supports loading. The Macaulay bracket is defined by the operation $2\langle x\rangle = x + |x|$. Interface properties used in the simulations, including fracture energies at $\theta = \theta_0$ for pure normal (γ_n) and pure tangential separation (γ_s) are listed in Table 2. As discussed in Clayton (2005b), the choice of

Table 2
Properties for interfacial fracture

Parameter	Value
$\hat{s}_0$ (GPa)	2.0
$\hat{s}_1$ (GPa/K)	0.01
$\hat{\tau}_0$ (GPa)	4.0
$\hat{\tau}_1$ (GPa/K)	0.01
δ_c (mm)	1.0
γ_n (kJ/m^2)	1.0
γ_s (kJ/m^2)	2.0

relatively large mode II toughness, $\hat{\tau}_0/\hat{s}_0 = 2$, prevented shear failure from occurring during propagation of the compressive pulse. Note that in what follows, the same fracture model and parameters are used to model intergranular fracture along W–W boundaries and interphase fracture at W-binder interfaces.

3.3. Numerical simulations

Constitutive models presented for bulk and interfacial responses, respectively, were implemented within an explicit Lagrangian finite element solver (Clayton, 2005b; Johnson et al., 2001). Two-dimensional calculations were conducted, with microstructures for meshing obtained from cross-sectional samples of a KE rod of the WHA material as shown in Fig. 1(a). Fields-of-view from three different microstructures were considered, as shown in Fig. 3, each a square window of size $L = 150\,\mu\text{m}$. The microstructure exhibiting nearly equiaxed grains is labeled transverse-1, whereas those with elongated grains are labeled axial and transverse-2, respectively. Note from the left image in Fig. 1(a) that the line-VISAR system is oriented perpendicular to the major axis of the ellipsoidal grains in microstructure axial. Microstructure transverse-2 was obtained by rotating the axial microstructure 90° clockwise. Realistic lattice orientations depending upon spatial location were obtained from EBSD measurements performed on the samples and were used as initial conditions in the simulations. It is expected that there would be some variation in microstructures reconstructed from EBSD measurements of other regions of the sample of material, but a comprehensive treatment of such variation is not considered in the current work. However, the initial lattice orientations used in the numerical simulations were representative subsets of those shown in Fig. 1(b); i.e., inverse pole figures for lattice orientations used in the simulations (not shown) appeared very similar to those in Fig. 1(b). Small gradients in initial lattice orientations within grains, evident in Fig. 1(a), were captured; i.e., grains were not initially homogeneous. The meshes of triangular elements conform to the microstructure and are selectively refined in the vicinity of grain and phase boundaries to better resolve fracture surfaces.

In Fig. 3 and henceforth, in-plane spatial coordinates will be denoted by the conventional notation $x = x^1$ and $y = x^2$. Analyses were plane strain in the x–y plane, representing columnar polycrystals extended infinitely in the out-of-plane direction. Out-of-plane elastic and plastic deformations were permitted so long as the total deformation field remained planar. The lower and upper edges of the domain are denoted by reference coordinates $Y = X^2 = 0$ and $Y = X^2 = L$, respectively. Left and right edges are denoted by $X = X^1 = 0$ and $X = X^1 = L$, respectively. Velocity initial and boundary conditions were prescribed as

$$\dot{x}|_{X=0} = \begin{cases} 0.5V_\text{I}\left(t/10^{-9}\,\text{s}\right) & \text{for}\,0 \leqslant t \leqslant 10^{-9}\,\text{s}, \\ 0.5V_\text{I} & \text{for}\,10^{-9}\,\text{s} \leqslant t \leq 10^{-8}\,\text{s}, \\ 0.5V_\text{I}\left(\left[\left(1.1\times10^{-8}\,\text{s}\right) - t\right]/10^{-9}\,\text{s}\right) & \text{for}\,10^{-9}\,\text{s} \leqslant t \leqslant 10^{-8}\,\text{s}, \\ 0 & \text{for}\,t \geqslant \left(1.1\times10^{-8}\,\text{s}\right). \end{cases} \tag{19}$$

Above, V_I is the impact velocity. The factor 0.5 arises since in the corresponding experiments, the particle velocity of the shocked material is half of the impact velocity due to symmetry between the impactor and

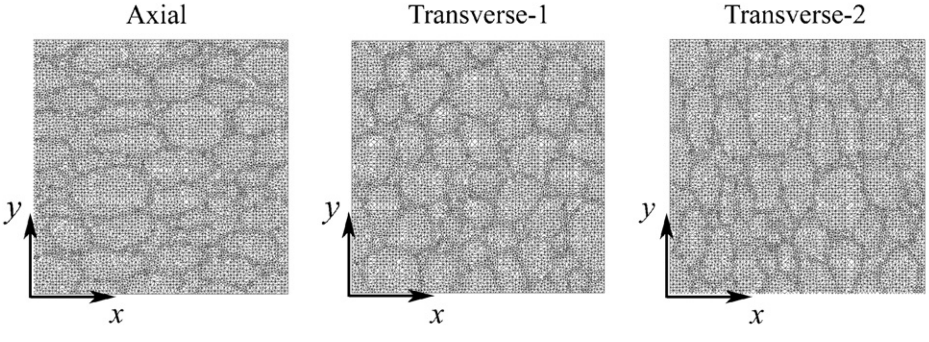

Fig. 3. Finite element meshes used in simulations.

Table 3
Numerical simulations

Simulation	Orientation	V_{I} (m/s)
WHA-I	Axial	350
WHA-II	Transverse-1	350
WHA-III	Transverse-2	250
WHA-IV	Transverse-2	350
WHA-V	Transverse-1	450

target materials. Note, however, that velocity boundary conditions (19) are not completely analogous to those of the two-body plate impact experiment, as will be apparent later upon examination of the local stress fields and free-surface velocities, for example. Conditions (19) result in a rightward-moving compressive pulse of approximate duration 9 ns. Additionally, boundaries along $Y = 0$ and $Y = L$ were free of shear stress but fixed in the y-direction, providing uniaxial conditions for in-plane strains, i.e.:

$$\begin{matrix} t^x = \sigma^{xy} n_y = 0 \\ \dot{y} = 0 \end{matrix} \quad \text{along} \quad \begin{cases} Y = 0, \\ Y = L. \end{cases} \tag{20}$$

Note that in plate impact experiment the macroscopic state of strain is uniaxial (i.e., no out-of-plane deformation), but local heterogeneities may induce out-of-plane deformations at the mesoscale. In the simulations, the right boundary was traction free, i.e., $\sigma^{ab} n_b = 0$ along $X = L$ for $t \geqslant 0$, mimicking the free surface at which the line-VISAR measurements are made. Null heat flux conditions were enforced along the external boundaries, with a uniform initial temperature $\theta_0 = 300\,\mathrm{K}$. Note that the present set of boundary conditions does satisfy periodicity in the y-direction, i.e., $y(Y = 0) = y(Y = L) = 0$.

Results from five spall simulations are discussed in Section 5. These are labeled with Roman numerals in Table 3 to distinguish them from the corresponding experiments labeled by number in Table 1. Parameters used in each simulation, specifically orientation of microstructure (Fig. 3) and impact velocity of Eq. (19), are shown in Table 3. Note that orientations axial and transverse-1 correspond to 2D projections of those grain orientations investigated in the experiments. Note also that numbers and numerals in Tables 1 and 3, respectively, differ in some cases with regards to microstructures and impact velocities for experiments 1–5 and simulations I–V. Some caution must be used when comparing results of 2D simulations with 3D experiments. For example, the in-plane microstructures used in experiments 3 and 4 (transverse-1), and simulations III and IV (transverse-2), differ visibly. However, effects of microstructure on spall fracture could be considered similar among these experiments and simulations, since all present relatively large grain boundary areas per unit volume perpendicular to the x-direction. This is in contrast to experiments 1 and 2 (Axial) and simulations I, II, and V (axial or transverse-1), which present relatively less grain boundary area per unit volume oriented nearly perpendicular to the loading direction.

4. Experimental results

The output of the line-VISAR was recorded on a Hadland Imacon 792 streak camera (experiments WHA-1 and 2) or a Hamamatsu H7700 streak camera (experiments WHA-3, 4, and 5). An example streak record is shown in Fig. 4. The vertical axis corresponds to position across the sample, while the horizontal axis is time t. Analyses were conducted as detailed previously (Trott et al., 2001) to yield velocity measurements at each bright line of the streak as well as three others equally spaced between the bright lines. In some cases, small amounts of data from the edge of the streak were discarded due to decreased image contrast or excessive noise. The result was a large set of free-surface velocities, $u_{\mathrm{p}} = \dot{x}|_{X=L}$, parameterized by time and position y across the sample. Small time corrections were made in the results to account for impactor tilt. This correction was done based upon a few contours of constant velocity in the middle of the initial shock wave. A time shift that was linear with position was performed so that these contours could be associated with constant arrival times.

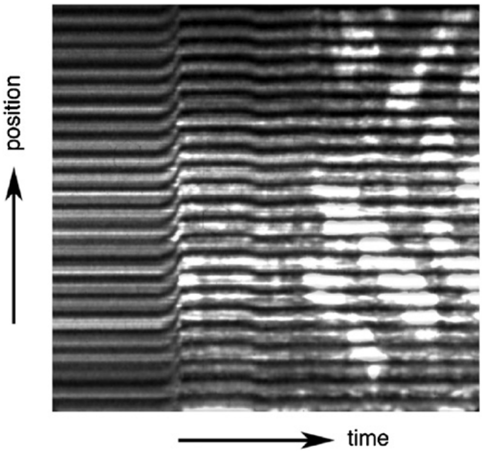

Fig. 4. Streak camera record from line-VISAR for experiment WHA-2.

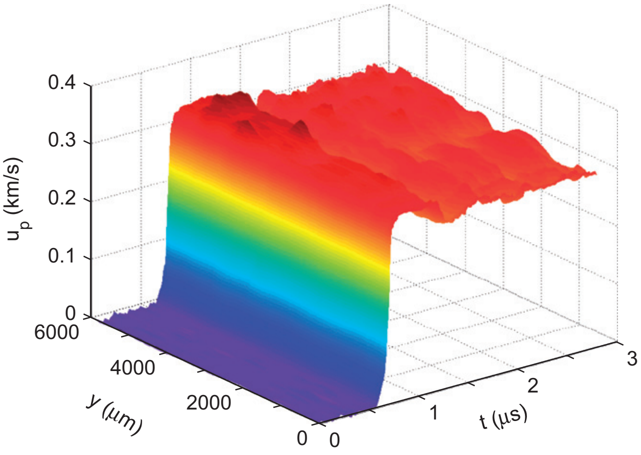

Fig. 5. Free-surface velocity history for experiment WHA-2.

The spatial resolution of the line-VISAR system as configured in these experiments was approximately 70 μm, meaning that the local free-surface velocities were recorded in 70 μm-spaced intervals in the *y*-direction.

4.1. Spatially resolved velocity measurements for experiment WHA-2

The results of one experiment, WHA-2, are examined here in detail and viewed in a variety of ways. Later, the results from all experiments will be analyzed and compared. The free surface velocity for test WHA-2 is plotted as a surface in *y*–*t* space in Fig. 5. While it is difficult to see features of the initial shock in this view, the initial flat top for the shocked state and the subsequent spall pullback signature are readily apparent. One can also clearly see variations in velocity along the *y*-direction.

By spatially averaging the measurements along the free edge at each time instant, an average particle velocity $\bar{u}_\mathrm{p}$ can be found as

$$\bar{u}_\mathrm{p} = \frac{1}{L}\int \dot{x}|_{x=L}\,\mathrm{d}y, \tag{21}$$

as shown in Fig. 6. In previous investigations of sugar (Trott et al., 2001, 2007a) and HMX (Trott et al., 2002), this average has been shown to have the same shock arrival and rise time as a conventional point VISAR

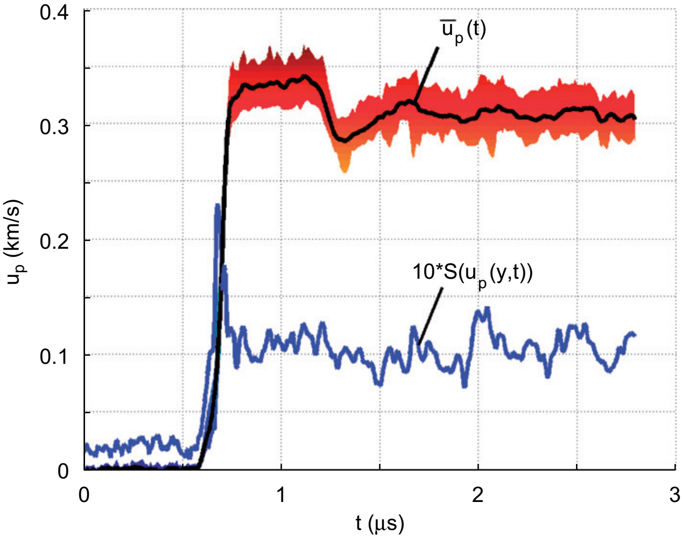

Fig. 6. Free-surface velocity history for experiment WHA-2: spatial average (black), spatial variation (red), and standard deviation (blue, magnified10 ×).

measurement, but significant variations between the two measurements were found after the shock arrival. Since it is difficult to correlate impact time to the VISAR measurement, the time of the records is adjusted so that the base of the average curve arrives at the measured ultrasonic sound speed of the material. Therefore, in Fig. 5 and subsequent plots, $t = 0$ corresponds to the instant of impact. From the average velocity history, it is possible to see the ramping elastic foot in front of the main shock wave consistent with previous VISAR measurements on WHA (Bless and Chau, 2006; Dandekar and Weisgerber, 1999). The elastic ramp is followed by a plastic (bulk) wave that also has a finite rise time. The bulk wave is followed by a region over which the particle velocity is relatively constant. At about 1.2 μs after impact, the particle velocity decreases as unloading waves arrive from the back of the impactor. Eventually, the interaction of unloading waves leads to tensile failure of the sample (spall), which appears as the increase in particle velocity as the fractured material accelerates relative to the remainder of the sample. Spall will be discussed in detail in Section 4.3. The remainder of the velocity record consists of wave reverberations within the spalled material with a period of slightly less than 1 μs.

The variation in particle velocity is illustrated in two ways in Fig. 6. First, the range of data obtained is shown as the colored (red) band above and below the average value. In general, the width of this band is nearly constant, though it is nearly invisible in the first shock. Second, the standard deviation of the velocities, $S(u_p(y,t))$, for a given time (scaled by a factor of 10 for clarity) is shown in blue. The velocity distributions for each time are relatively normal in character, though for 20–40% of the data after the initial arrival of the wave a normal distribution does not describe the data well as the null hypothesis can be rejected at the 95% confidence level based on the χ^2 test. For this experiment, the standard deviations are nearly invariant with respect to time except at the initial shock front. There, relatively small differences in the arrival time of the wave can result in fairly large deviations from the average. This behavior is quite similar to that seen in experiments on sugar (Trott et al., 2007a) except the peak to plateau ratio is 4–5 for sugar and 2–2.5 in this experiment. The variations in particle velocity prior to arrival of the main shock provide an indication of the noise inherent in the line-VISAR. The baseline variation is 10–20% of the steady-state variation.

Temporal variations in the arrival of the initial shock wave can be seen more readily by viewing velocity contours in the y–t plane as shown in Fig. 7. The contours are clearly variable across the width of the specimen, with the variation being largest for low (0.05 km/s) and high (0.30 km/s) velocity contours. Variability at the low velocity is likely due to local differences in matrix concentration or crystallographic orientation of the grains. The variation at the higher velocity is only larger in the region of $y = 0$–1000 μm. For contours between these extremes, the spatial variation is comparable. In general, these variations have periods

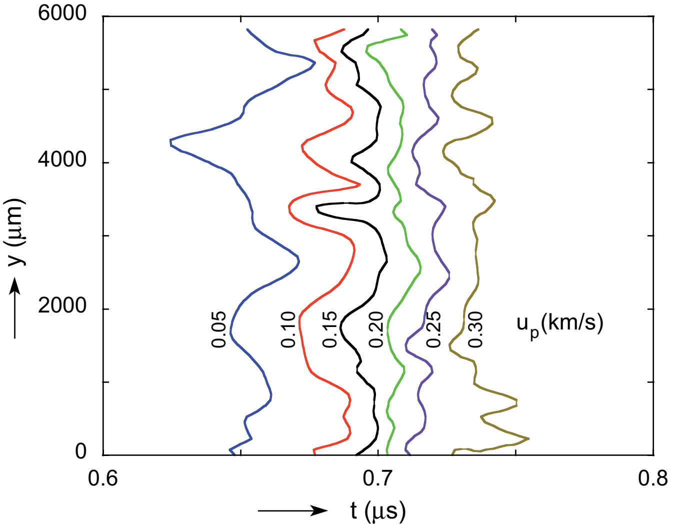

Fig. 7. Contours of constant free-surface velocity of shock front in y–t plane for experiment WHA-2.

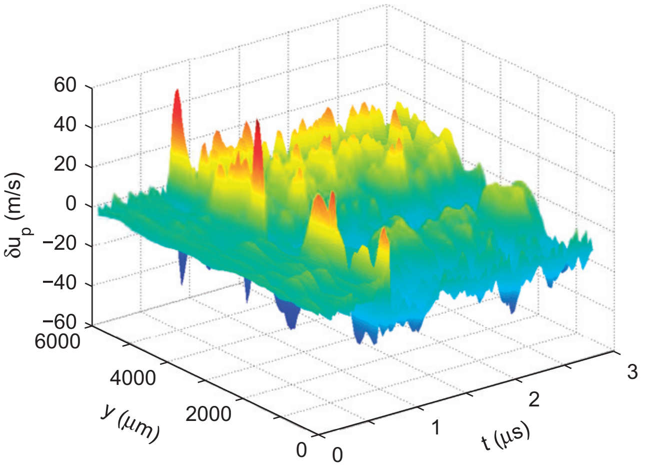

Fig. 8. Perturbations of free-surface velocity for experiment WHA-2.

on the order of 1 mm, significantly larger than the sizes of individual grains. Thus, the variations are thought to be caused by variations in elastic and plastic properties of ensembles of grains for some depth below the free surface at which measurements are made.

By subtracting the spatially averaged velocity of Fig. 6 from the local velocities in Fig. 5, i.e.,

$$\delta u_p(y,t) = u_p(y,t) - \bar{u}_p(t), \tag{22}$$

we obtain the spatially resolved velocity deviations (δu_p) shown in Fig. 8. Significant peaks and valleys exist, especially near the arrival of the first shock, but dominant spatial and temporal scales in the velocity deviations are absent, in contrast to those previously observed in shock-loaded boron carbide (Vogler et al., 2004).

4.2. *Effect of impact velocity and sample orientation*

Effects of impact velocity and sample orientation can be deduced from the spatially averaged free-surface velocities shown in Fig. 9. As the impact velocity increases, the rise time for the main (bulk) shock wave

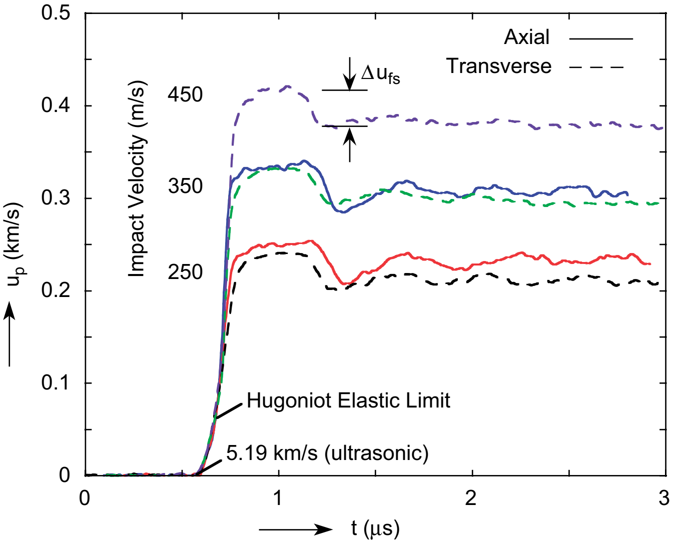

Fig. 9. Spatially averaged free-surface velocity histories for all experiments.

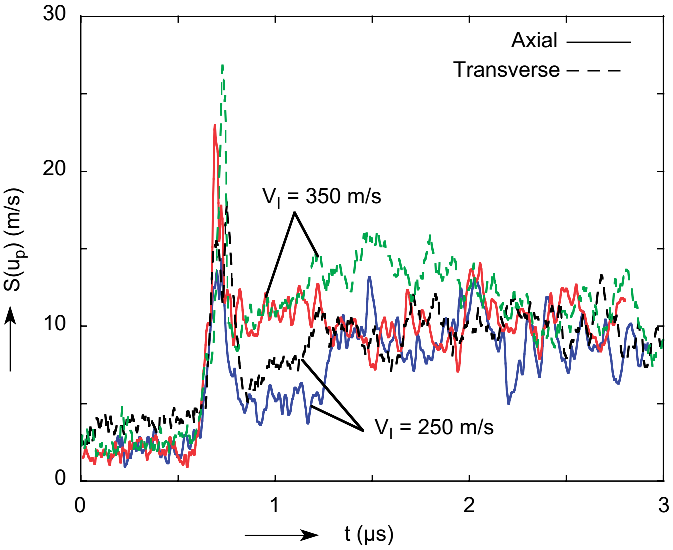

Fig. 10. Standard deviation in free-surface velocities for experiments WHA 1-4.

decreases as expected, but the transversely oriented samples have longer rise times than axially oriented ones. The edges of the plateau velocity region are more rounded for the transverse samples, and, although not visible in this figure, the elastic foot is more spread out for the transverse samples. The pullback associated with spall is somewhat smaller for the transverse experiments, as is ringing in the spalled plate.

The standard deviations of velocity versus time for experiments 1–4 are compared in Fig. 10. As seen previously in Fig. 6 for WHA-2, a significant peak in the velocity dispersion occurs at the shock front. This peak is about 25 m/s for impacts at 350 m/s versus about 15 m/s for 250 m/s impacts, with somewhat higher peaks for the transverse samples. After the peak, a plateau in dispersion exists until about 1.2 μs, with the value of the plateau of the 250 m/s experiments about half that of the 350 m/s experiments. This time (1.2–1.3 μs) corresponds to the decrease in particle velocity associated with unloading (the pullback signature). The dispersion of the experiments with 250 m/s impact velocity then increases to

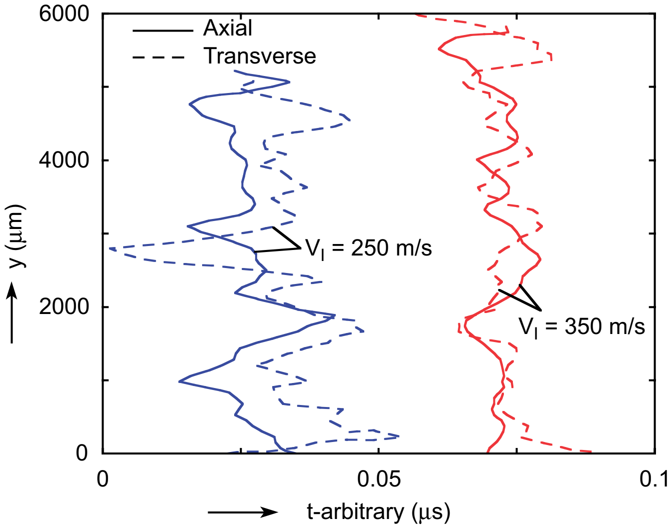

Fig. 11. Contours of constant free surface velocity ($V_I/2$) of shock front in y–t plane for experiments WHA 1-4.

about 10 m/s, while the dispersion levels in experiments of 350 m/s impact velocity remain constant or increase only slightly.

As was the case for WHA-2 (Fig. 8), contours of the velocity at the shock front are non-uniform for experiments 1–4 as shown in Fig. 11. The contours shown are of constant free-surface velocities equal to half the impact velocity (i.e., 125 m/s and 175 m/s). The fluctuations in the contours decrease for the higher impact velocity (350 m/s), consistent with the decreasing rise times that occur for the spatially averaged responses. In fact, the local variations in the front contribute significantly to the rise time for the averaged response. The fluctuations are also higher and the contours more jagged for transverse than for the axial experiments at the same impact velocity. Standard deviations, S_t, for the temporal positions of the contours are 6.0, 3.8, 10.1, and 5.9 ns for WHA-1 to WHA-4, respectively. For both sample orientations, the ratio of S_t for experiments at 350 m/s to those at 250 m/s is approximately 0.6, suggesting a scaling that is invariant to orientation. Approximately, the same ratio is found when comparing S_t for axial and transverse samples.

4.3. Hugoniot results

The macroscopic deformations of the WHA samples were determined from the average free-surface velocity histories using the Rankine–Hugoniot jump conditions for conservation of mass and momentum across a steady wave, though the steadiness of the waves has not been verified experimentally. Because the shock wave separates into elastic and plastic components, it must be analyzed in two steps as described, e.g., in Vogler et al. (2004). In all cases, impact was assumed to be symmetric so that the particle velocity of the shocked material is half of the impact velocity. This assumption is acceptable since the macroscopic mechanical responses of the longitudinal impactors and transverse samples are roughly equivalent. The Cauchy stress ($\sigma = \sigma^{11}$)–volumetric strain ($\varepsilon = \rho_0/\rho - 1$) behavior for the current experiments, along with that from Dandekar and Weisgerber (1999), are shown in Fig. 12 and listed in Table 1. The current results agree with the earlier results except for experiment WHA-5, which is probably due to the aforementioned difficulties with that experiment affecting the accuracy of that measurement. For the other impact velocities, the macroscopic responses of the transverse samples were slightly more compliant than their longitudinally oriented counterparts, possibly a result of anisotropic work hardening during processing or grain elongation in the longitudinal direction. The HEL deduced from the average free-surfaces velocities for the five current experiments varies widely. This is largely due to the spread out nature of the elastic wave and lack of a distinct break associated with yielding. Indeed, after consulting individual velocity records from a given experiment, a wide range of waveforms was observed. This variability may be due to fluctuations in phase composition or

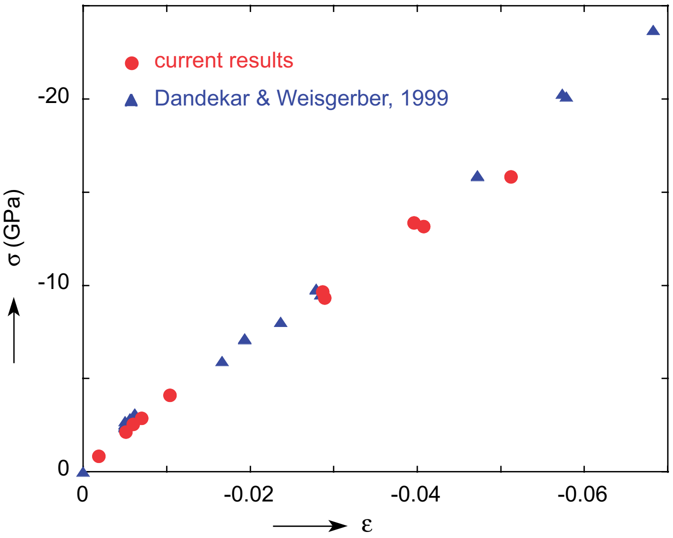

Fig. 12. Overall compressive stress-engineering strain response showing elastic limit (HEL) and Hugoniot states for current experiments and from Dandekar and Weisgerber (1999).

grain orientations among vicinities where local measurements were made. The average of the value of the HEL for all five experiments is 2.5 GPa, with most of the values close to that. This is in reasonably good agreement with the value of 2.76 GPa obtained previously for a similar material (Dandekar and Weisgerber, 1999).

Recall from Fig. 1(b) that the microstructures exhibited a slight preference for alignment of $\langle 1\,1\,0 \rangle$ axes in the W grains in the direction of extrusion, i.e., along the x-axis in the axial samples and along the z-axis (out-of-plane) in the transverse samples. Zhou (1993) found that cross rolling increased the flow stress of WHA under high pressure–shear loading (at nominal shear strain rates on the order of $10^3\,\mathrm{s}^{-1}$), though crystallographic textures were not discussed explicitly in that investigation. Subhash et al. (1994) found that pure polycrystalline W samples with preferred $\langle 1\,1\,0 \rangle$ orientations tended to be somewhat more compliant under high-rate compressive loading (at strain rates up to the order of $10^4\,\mathrm{s}^{-1}$) than those with preferred $\langle 1\,0\,0 \rangle$ orientations. In the present work, on the other hand, a slight decrease in compliance of the axial oriented samples (i.e., higher value of σ_h in Table 1) containing a preference for $\langle 1\,1\,0 \rangle$ texture was found. The role of crystallographic texture on the flow stress of the FCC binder phase has not, to the authors' knowledge, been investigated experimentally. However, as will later be demonstrated in the simulations, much of the plastic deformation occurring during impact loading appears to be accommodated by the more ductile binder phase, and hence the inelastic behavior of the binder may strongly influence the overall response of the composite.

4.4. Statistics of spall strength

Dynamic tensile failure in uniaxial strain loading, typically referred to as spall or spallation, frequently occurs in impact events, including the current plate impact experiments. A thorough discussion of spall phenomena can be found in Antoun et al. (2003). The spall strength of a similar variety of WHA to that currently studied has been measured to be 1.7–2.0 GPa (Dandekar and Weisgerber, 1999). In a typical spall experiment, impact sends a shock wave (or elastic and plastic waves, depending upon stress level) through both the target and impactor. Propagation of these and subsequent waves is shown schematically in Fig. 13, and the states of the material in the stress–particle velocity plane are shown in Fig. 14. The initial shocked state, defined by stress and particle velocity σ_h and $u_\mathrm{h} = 0.5V_\mathrm{I}$, is labeled as I in this figure. When the compression waves reach the back of the target, a stress-free surface, and the back of the impactor, which has a low-impedance material against it, most or all of the wave reflects as an unloading wave. This unloading wave from the free surface at the back of the target, also referred to as a rarefaction fan because of its tendency

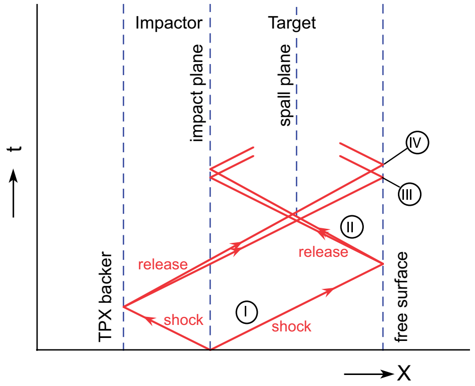

Fig. 13. Schematic of wave propagation in a plate impact spall experiment.

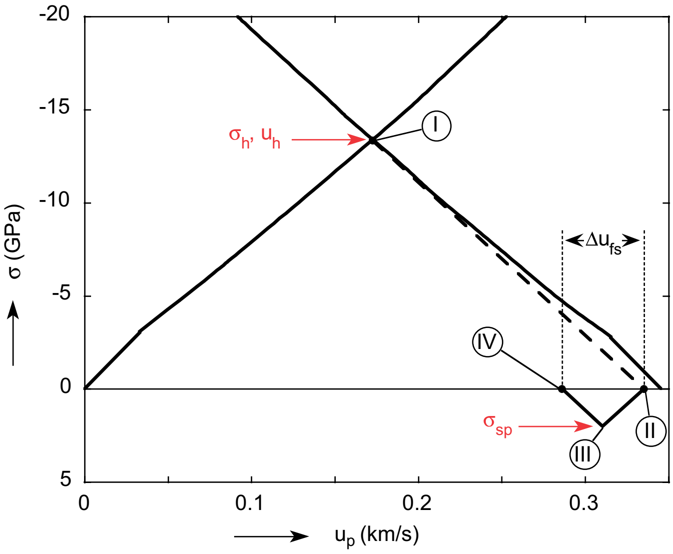

Fig. 14. Schematic of average stress states in target material during a plate impact spall experiment.

to spread as it propagates, unloads the sample to zero stress and the particle velocity shown as II. Note that this free-surface velocity is somewhat lower than the impact velocity due to hysteresis associated with plastic deformation and other dissipative mechanisms. When the two rarefaction fans begin to intersect one another, they load the material into tension. If the rarefactions are of sufficient magnitude, the material will fail dynamically in tension (III) and unload to zero stress (IV). For the current experimental setup with a target to impactor thickness ratio of 2:1, tensile failure will occur in the vicinity of the midplane of the target as shown in Fig. 13. If the impedance of the material in tension is known, the spall strength can be determined from the so-called free-surface pullback velocity Δu_{fs} (see Fig. 9). However, the instantaneous impedance is typically not known when the material deforms plastically. Dandekar and Weisgerber (1999) attempted to determine the impedance of WHA directly through concurrently backing the target material with void and PMMA. By assuming the same spall strength is reached in the two cases, the impedance can be found. However, we shall see that significant variations in the apparent spall strength for various positions render the validity of this assumption questionable. Instead, in the current investigation we calculated the slope (impedance) from the shocked state (I) to the unloaded state (II) in the σ-u_{p} plane of Fig. 14 and assumed the same slope in the tensile regime.

The results for experiment WHA-2 are first examined in detail, and then differences between this test and the other experiments are considered. The average peak particle velocity u_1, the pullback velocity u_2, and their difference Δu_{fs} are shown versus position y in Fig. 15. Clearly, the pullback velocity varies considerably with position in the sample. Utilizing the unloading slope, U_t, as described above, the local spall strength can be calculated as

$$\sigma_{sp} = \rho_0 U_t \Delta u_{fs}/2. \tag{23}$$

The impedance $\rho_0 U_t$ assumed for this experiment of 82 $\text{Gg/m}^2\text{s}$ is higher than the range of 64–76 $\text{Gg/m}^2\text{s}$ found by Dandekar and Weisgerber (1999) but lower than the value of 92 $\text{Gg/m}^2\text{s}$ one would use if an elastic wave were assumed. The probability distribution of these spall strengths is shown in Fig. 16. The average

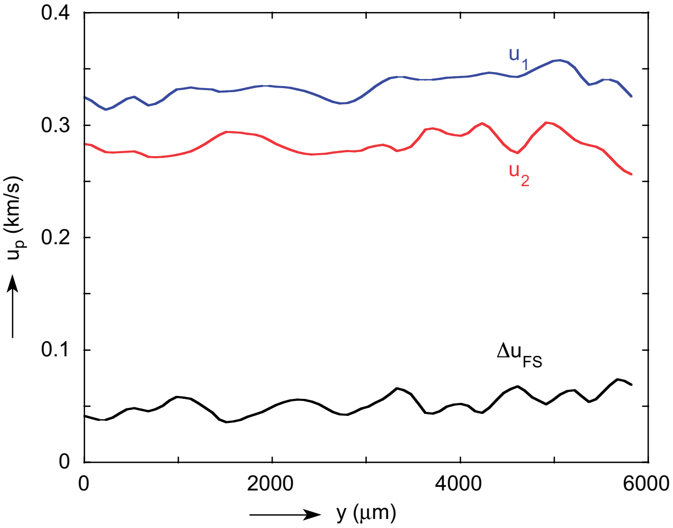

Fig. 15. Spatially resolved peak particle velocity (u_1-blue), pullback velocity (u_2-red), and their difference (Δu_{fs}-black) for experiment WHA-2.

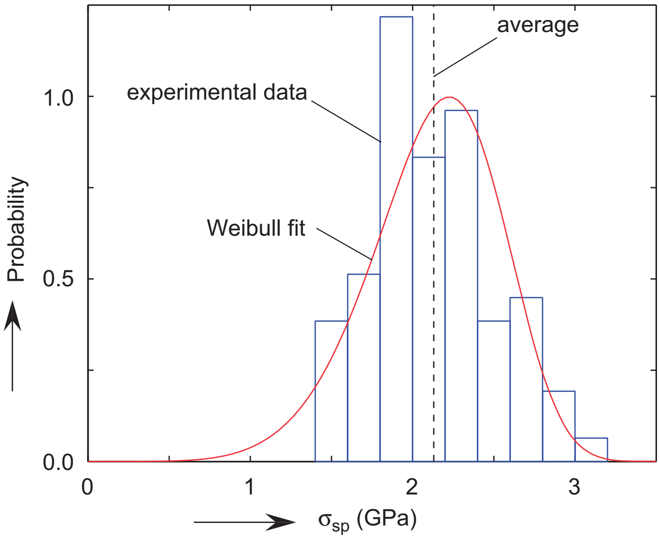

Fig. 16. Probability distribution of spall strength and Weibull fit for experiment WHA-2.

Table 4
Statistical parameters for experimental spall strengths

Expt.	U_t (km/s)	$\sigma_{sp}(\bar{u}_p)$ (GPa)	Normal distribution		Weibull distribution	
			$\bar{\sigma}_{sp}$ (GPa)	$S(\sigma_{sp})$ (Gpa)	σ_0 (GPa)	β
WHA-1	4.34	1.62	1.85	0.31	1.98	6.92
WHA-2	4.62	2.01	2.13	0.37	2.29	6.13
WHA-3	4.48	1.55	1.66	0.32	1.79	6.00
WHA-4	4.70	1.55	1.70	0.33	1.84	4.99
WHA-5	4.36	1.59	1.98	0.61	2.20	3.46

value of spall strength for this experiment is $\bar{\sigma}_{sp} = 2.13$ GPa, somewhat larger than the spall strength $\sigma_{sp}(\bar{u}_p) = 2.01$ GPa inferred from the spatially averaged particle velocity. The averaging of particle velocities tends to smooth out local particle fluctuations so that u_2 is higher and u_1 is lower in the spatially averaged case. The standard deviation of the spall strengths for this experiment, $S(\sigma_{sp})$, is 0.37 GPa. Such a large value may explain why significant variations are sometimes seen in spall experiments on the same material (Baoping et al., 1994; Bless and Chau, 2006; Dandekar and Weisgerber, 1999). As it is customary to represent reliability and strength of mechanical parts with Weibull distributions (Weibull, 1951), a Weibull fit to the spall data, performed using the maximum likelihood method (Bury, 1975), is also shown in Fig. 16. We note, though, that there is no statistical support for choosing a Weibull distribution over a normal distribution for this data. The first Weibull parameter, σ_0, is close to the average, while the modulus, β, is 6.13. Weibull moduli of 5.5 for flexure and 6.9 for tension of sintered tungsten have been reported elsewhere (Margetson and Sherwood, 1979). Recall that the lower the Weibull modulus β the greater the scatter in the data.

We note that Eq. (23) follows from the assumption of planar deformation in the sample, but this is clearly not the case as illustrated in Figs. 7 and 11. Waves propagating through intact material develop non-uniformities due to the heterogeneous microstructure and material anisotropy, and the failure process itself will introduce additional deviations from planar behavior as failure occurs at different times and depths for different positions in the tensile-loaded region. Since all materials with microstructure are expected to display non-planar shock waves and even single crystals will probably experience local differences in failure strength due to intragranular defects, all spall experiments are expected to have some degree of non-planarity. Nevertheless, spall strengths are inevitably calculated using Eq. (23) or some variant on it (Antoun et al., 2003; Baoping et al., 1994; Dandekar and Weisgerber, 1999), almost always with no knowledge or consideration of non-planarity. Thus, caution should be used in relating pullback velocities to the spall strength of the material, not only for the current investigation but for all spall experiments. Decoupling the effects on the distributions due to the two sources (initial microstructure and induced failure) is difficult, but some insight can be gained from the current experiments and simulations.

Spall parameters obtained from all experiments are given in Table 4. The average spall strengths $\bar{\sigma}_{sp}$ for transversely oriented samples (WHA-3 and 4, grains elongated perpendicular to the loading axis) are generally 10–20% lower than for the axially oriented samples (WHA-1 and 2, grains elongated parallel to the loading axis) at the same impact velocity. A possible explanation for this effect, upon consideration of the microstructure and numerical results, will be given later in Section 6. The standard deviation and Weibull modulus, though, are about the same at 0.31–0.37 GPa and 5–7, respectively, for all experiments except WHA-5, which exhibits more spatial variability. For reasons explained above, the spall strength from the average particle velocity, $\sigma_{sp}(\bar{u}_p)$, is always lower than the average spall strength $\bar{\sigma}_{sp}$.

5. Numerical results

Recall that boundary conditions listed in Eq. (19) result in a compressive stress wave moving from left to right in the microstructure, i.e., the positive X-direction. This wave reflects off the free surface at $X = L$ at around $t = 37$ ns, producing a release wave and leading to initiation of spall at around $t = 40$ ns.

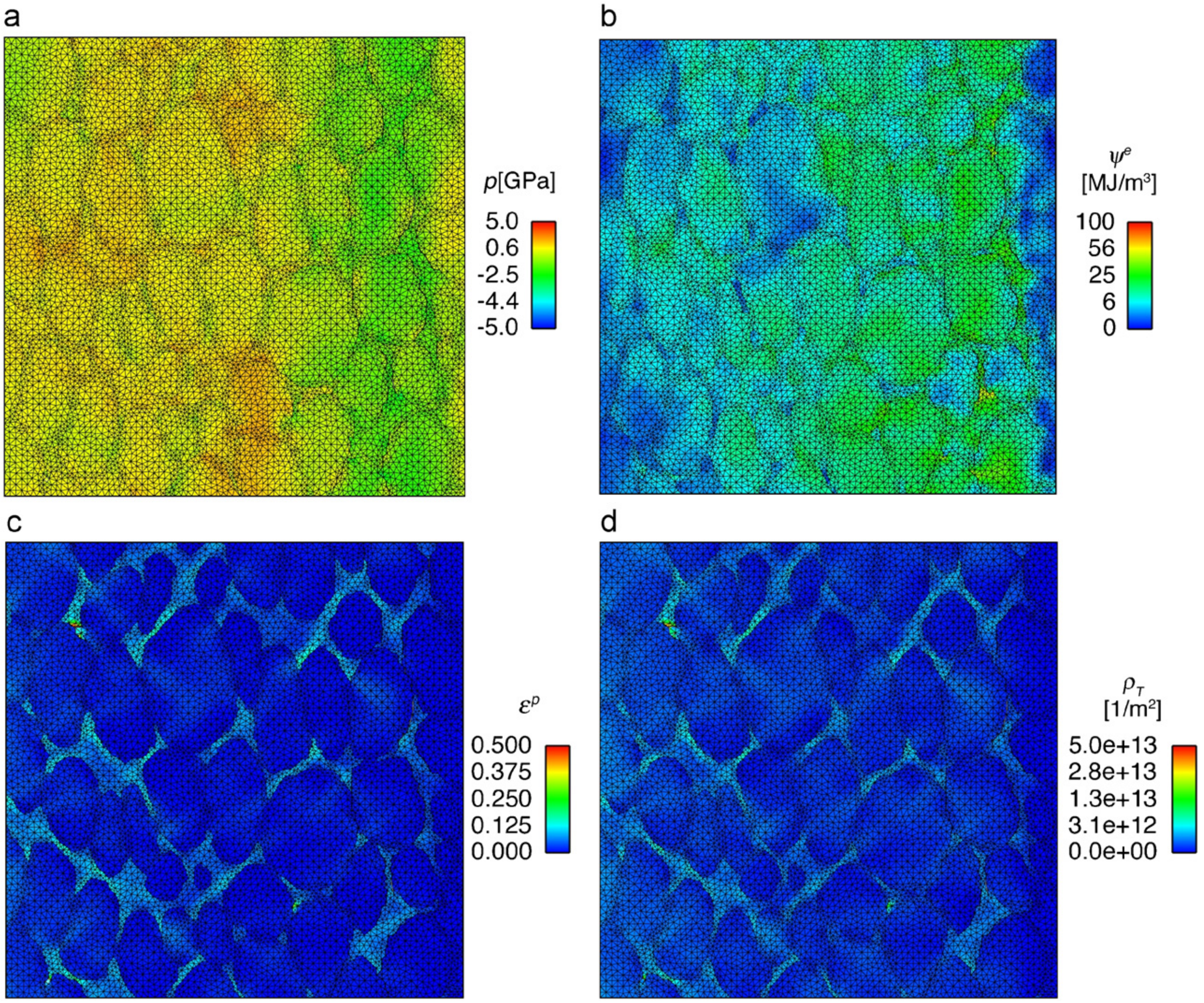

Fig. 17. Field variables for simulation WHA-III at $t = 40\,\mathrm{ns}$ (~initiation of spall): (a) pressure; (b) elastic energy density; (c) cumulative plastic strain; and (d) dislocation density.

5.1. Field variables and damage

Contour plots of Cauchy pressure p (mean stress), elastic energy density ψ^{e}, cumulative plastic strain ε^{p}, and dislocation density ρ_{T} are shown in Figs. 17 and 18 for simulations WHA-III and IV, respectively. These variables are defined by

$$p = -\mathrm{tr}(\boldsymbol{\sigma})/3, \tag{24}$$

$$\psi^{\mathrm{e}} = K_0(\theta)\vartheta^2/2 - K_1\vartheta^3/3 + \mu(\theta)\mathbf{e}^{\mathrm{e}'}:\mathbf{e}^{\mathrm{e}'} \tag{25}$$

$$\varepsilon^{\mathrm{p}} = \int \sqrt{(2/3)\mathbf{d}^{\mathbf{p}}:\mathbf{d}^{\mathbf{p}}}\,\mathrm{d}t, \quad \mathbf{d}^{\mathbf{p}} = \mathrm{sym}(\mathbf{l}^{\mathbf{p}}), \tag{26}$$

$$\rho_{\mathrm{T}} = \left[(\hat{\alpha}\mu(\theta_0)bn)^{-1}\sum_{\alpha=1}^{n}\left(g_0^{(\alpha)} - g_y^{(\alpha)}\right)\right]^2. \tag{27}$$

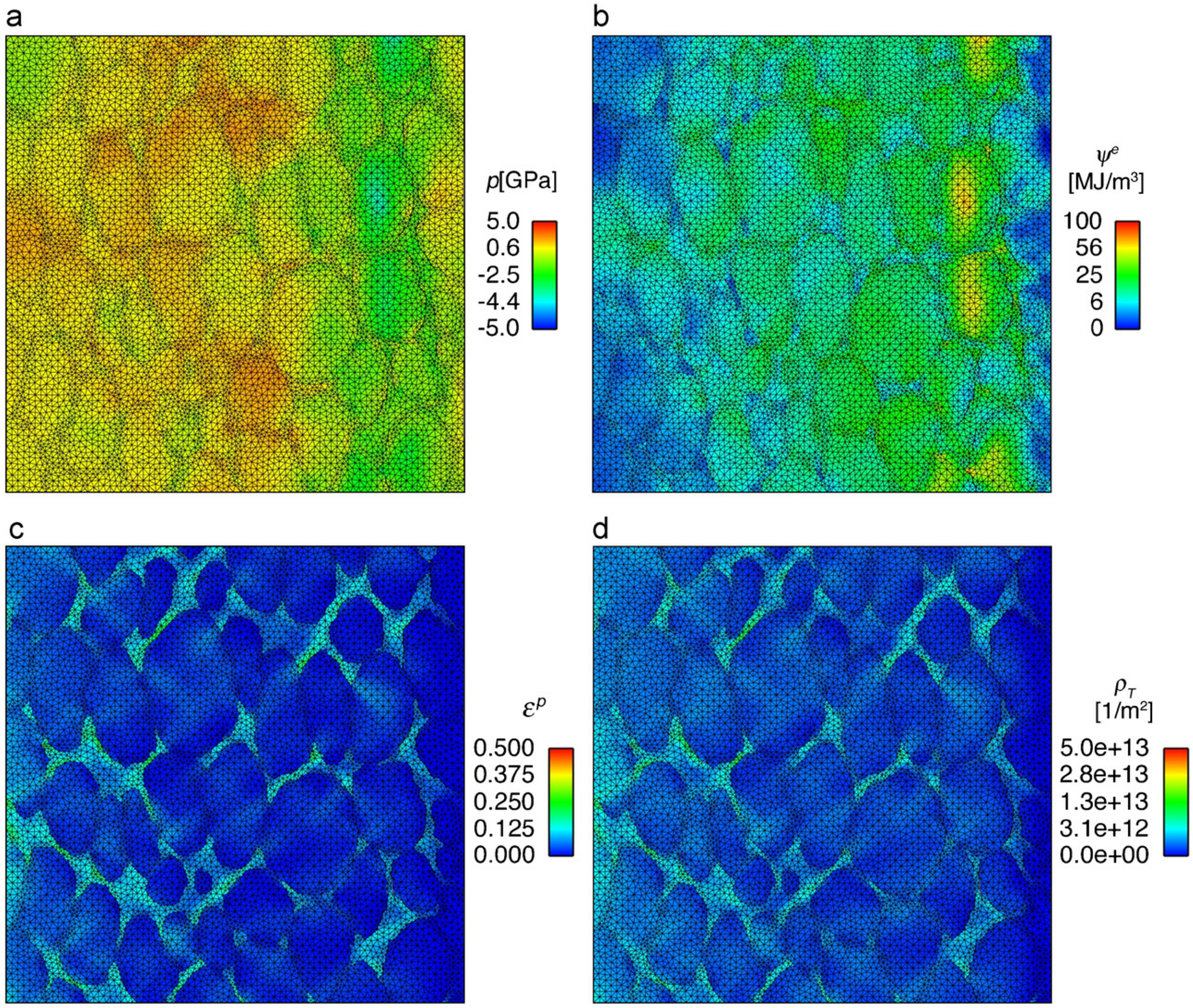

Fig. 18. Field variables for simulation WHA-IV at $t = 40\,\text{ns}$ (~initiation of spall): (a) pressure; (b) elastic energy density; (c) cumulative plastic strain; and (d) dislocation density.

The same color scales are used in Figs. 17 and 18 to facilitate comparison. Note that regions of large tensile pressures develop near the impending spall plane, towards the right quarter of each sample. Correspondingly, large elastic energies occur in the same regions. Plastic strains tend to be largest in the more ductile matrix phase, which also undergoes more strain hardening and dislocation accumulation. Comparing Fig. 17 (WHA-III, impact velocity 250 m/s) with Fig. 18 (WHA-IV, impact velocity 350 m/s), local pressures, energies, plastic strains, and dislocation densities all generally increase with increasing magnitude of the impact velocity. Note also that over the time duration of the simulations, local plastic strain rates on the order of $\dot{\varepsilon}^{\mathrm{p}} = 10^7\,\mathrm{s}^{-1}$ were attained (i.e., plastic strains in excess of 0.1 were achieved over time periods on the order of ~10 ns).

Contours of effective stress σ^{eff} are shown for all simulations, after spall has occurred, at $t = 60\,\text{ns}$ in Fig. 19 and $\text{t} = 80\,\text{ns}$ in Fig. 20. The effective stress in Figs. 20 and 21 is defined as follows in terms of the deviatoric Cauchy stress:

$$\sigma^{\mathrm{eff}} = \sqrt{(3/2)\boldsymbol{\sigma}' \colon \boldsymbol{\sigma}'}. \tag{28}$$

Notice that effective stresses relax as a result of fracture, as indicated by slightly lower stress values, in general, in the microstructures of Fig. 20 relative to the same microstructures in Fig. 19. However, comparing results

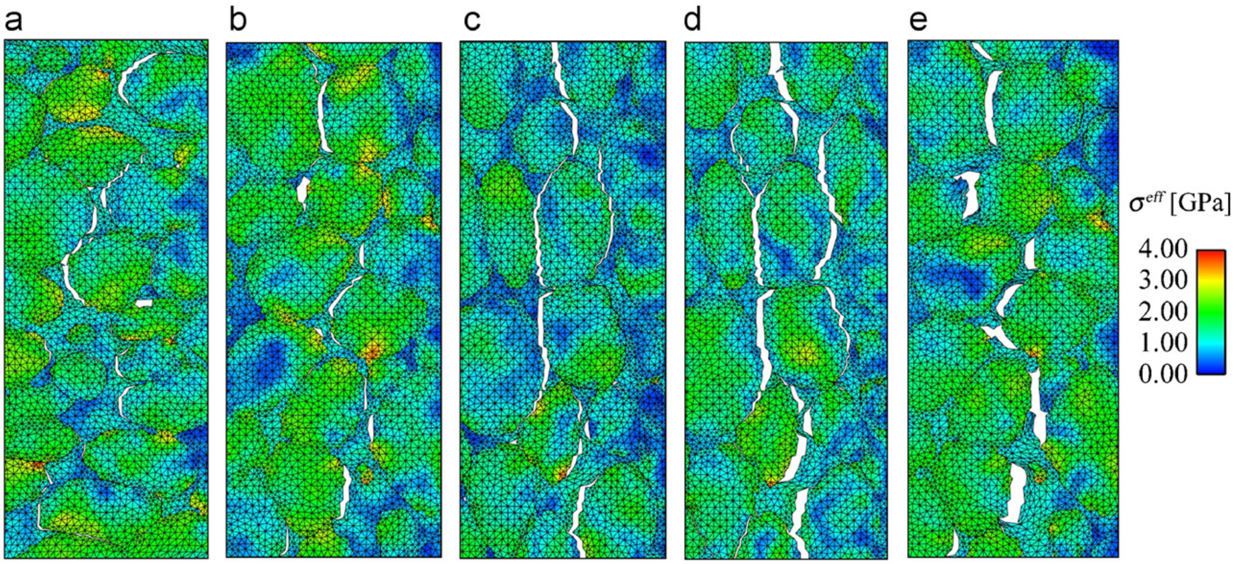

Fig. 19. Effective stress near spall planes at $t = 60\,\mathrm{ns}$ from simulations: (a) WHA-I; (b) WHA-II; (c) WHA-III; (d) WHA-IV; and (e) WHA-V.

for the same microstructures conducted at different impact velocities, spall fracture tends to be more complete and more severe with increasing impact velocity, with larger local element distortion and generally larger crack opening displacements. For example, fracture is more severe in simulation WHA-V (450 m/s) than WHA-II (350 m/s), and is more severe in WHA IV (350 m/s) compared to WHA-III (250 m/s). Note that fracture occurs most readily for simulations of the transverse-2 microstructure, WHA-III and IV, with apparently the largest number of available grain boundary facets per unit area oriented nearly perpendicular to the wave propagation direction. Also, notice that the spall fracture planes do not cut cleanly across the material, but rather ligaments of highly stretched material hold the sample together where insufficient grain boundary facets (i.e., cohesive finite elements in the numerical context) exist to propagate cracks across the domain. Presumably, in an actual material, cleavage fracture (absent in the present model) would facilitate complete spall fracture of the sample. While the stress levels seen here are far below the ideal tensile strength (~30 GPa) of a perfect tungsten lattice (Roundy et al., 2001), microscopic flaws within the W grains or along their edges may enable cleavage under the present loading conditions, particularly along {1 0 0} and {1 1 0} planes known to be preferred orientations for grain cleavage (Gumbsch et al., 1998). Such flaws may be created during processing or the initial shock loading of the material.

Two quantitative indicators of the degree of damage induced in the sample by micro-cracking are specified as follows:

$$\Gamma = \sum_j \left(l\sqrt{\delta_\mathrm{n}^2 + \delta_\mathrm{t}^2} \right)^{(j)}, \quad \Omega = A^{-1} \sum_k (l)^{(k)}, \tag{29}$$

where summation for Γ is invoked over j micro-crack segments of length l, with crack opening displacement $\delta = \sqrt{\delta_\mathrm{n}^2 + \delta_\mathrm{t}^2}$. For Ω, summation is invoked over k micro-cracks satisfying the fully opened criteria $\delta \geqslant \delta_\mathrm{c}$, and $A = L^2$ is the area of the simulation domain. For purely normal separation, Γ is the 2-D analog of the total volume of free or void space in the sample produced during spall, and Ω is the scalar crack density (i.e., crack length per unit area). As indicated by the value of Γ in Fig. 21(a), significant damage evolution commences around $t = 40\,\mathrm{ns}$ in all simulations. Damage accumulates at the slowest rates in simulations I and II, as can be deduced from visual inspection of Figs. 19 and 20. The largest crack opening displacements occur in simulations IV (elongated grains oriented perpendicular to loading at intermediate velocity of 350 m/s) and V (equiaxed grains with highest impact velocity of 450 m/s). As shown in Fig. 21(b), numerous cracks do not

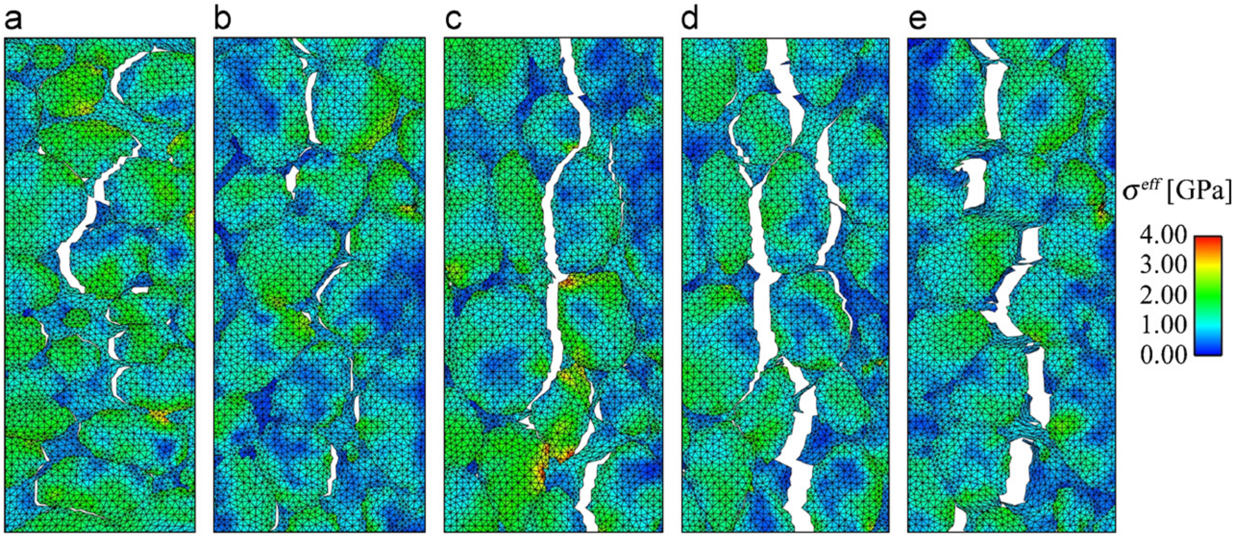

Fig. 20. Effective stress near spall planes at $t = 80$ ns from simulations: (a) WHA-I; (b) WHA-II; (c) WHA-III; (d) WHA-IV; and (e) WHA-V.

reach a fully opened state, $\delta \geqslant \delta_c$, in the simulations until around $t = 50$ ns. Also evident from Fig. 21(b), the largest crack densities accumulate in simulations of microstructure Transverse-2, cases WHA-III and IV. Some crack closure occurs in simulation WHA-II, for example, as evidenced by fluctuations (in particular, small local reductions) in Ω with increasing simulation time.

5.2. *Wave propagation and free-surface velocities*

As was done for the experiments, free-surface velocity statistics are first investigated here in detail for one simulation (WHA-IV), then in general for all simulations. The free-surface velocity history, $u_p(y, t)$ for WHA-IV is shown in Fig. 22. Note that the peak local free-surface velocity only reaches 311 m/s at $t = 36$ ns, even though the impact velocity V_I of Eq. (19) was 350 m/s. This phenomenon is attributed to attenuation of the initial loading wave by the fixed boundary condition in (19) for $t > 10$ ns and energy dissipation from inelastic deformation during wave propagation. If the impact velocity were held fixed at 350 m/s over the full duration of the simulation, eventually the free surface would attain a rigid-body velocity of 350 m/s once wave reflections were to subside. Spatial fluctuations in u_p with spacing on the order of the grain size, 10–30 μm, or even smaller, are apparent in Fig. 22 and in the plot of the velocity perturbation $\delta u_p(y, t)$ in Fig. 23. Significant fluctuations initiate at around 37 ns, when the maximum velocity is achieved at the free surface, and reach their largest magnitude around 45 ns (post spall). Contours of free surface-velocity in the y–t plane are shown in Fig. 24, analogous to the plot of experimental data in Fig. 7. Heterogeneities in the wave shapes on the order of the grain size are apparent in the initial elastic wave (50 m/s) and for low velocity contours (100–200 m/s). Heterogeneity increases drastically as a result of heterogeneous plastic deformation at later times, i.e., for $t > 34$ ns.

Spatially averaged free-surface velocity histories, $\bar{u}_p$, are shown in Fig. 25. Generally, the higher the impact velocity is, the higher the peak velocity or maximum value of $\bar{u}_p$ is over the duration of the simulation, as expected. Differences between average particle velocity curves corresponding to the same impact velocity are due to differences induced by the microstructure. For example, localization and heterogeneous plastic strain lead to different peak velocities among simulations II and IV, while final velocities at $t = 80$ ns differ due to different spall behavior. Note that nonzero free-surface velocities at late times are a result of the motion of the ejected, separated, or spalled material. Standard deviations, $S(u_p)$ in free-surface velocity are depicted in Fig. 26. For a given microstructure, the higher the impact velocity, the greater the dispersion or variance in particle velocity. For example, compare WHA-III (generally lower S, impact velocity of 250 m/s) with

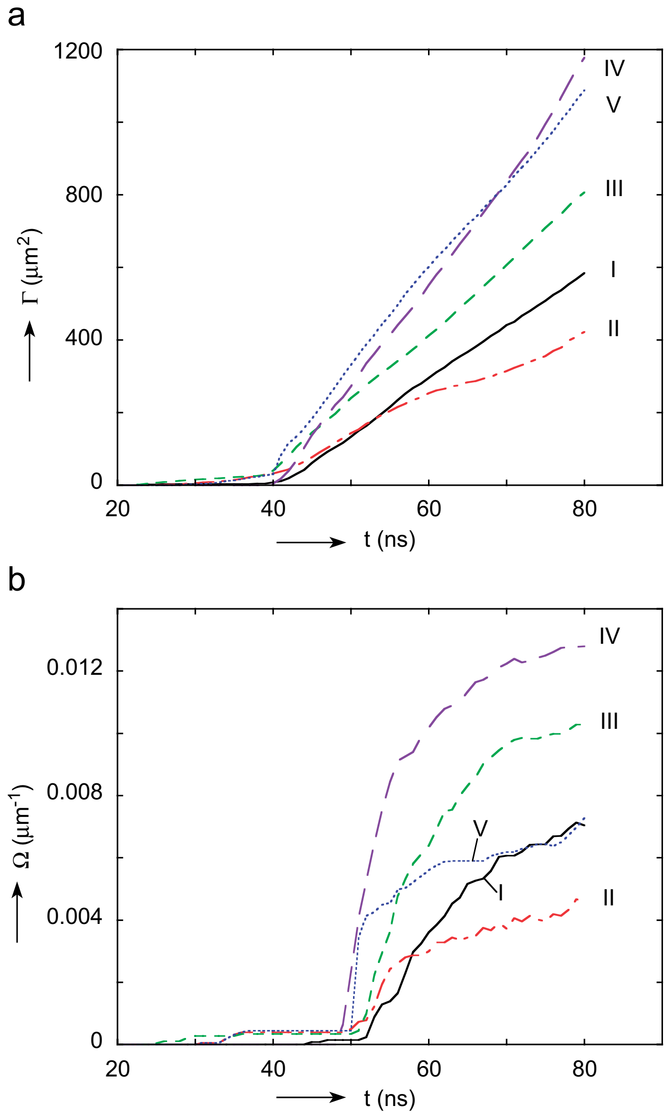

Fig. 21. Cumulative damage from micro-cracking: (a) summed product of crack length and opening displacement and (b) density of fully opened cracks ($\delta \geqslant \delta_c$).

WHA-IV (higher S, 350 m/s), or WHA-II (lower S, 350 m/s) with WHA-V (higher S, 450 m/s). This result is expected considering the character of the spall planes shown in Figs. 19 and 20. At a fixed velocity of 350 m/s, simulations with microstructure transverse-1 (WHA-II) tended to exhibit the smallest $S(u_\mathrm{p})$, perhaps because its nearly equiaxed grains produced the least spatial variation in response. Shown in Fig. 27 are contours of constant free-surface velocities for all simulations, analogous to the experimental data in Fig. 11. Here, traces of constant velocity $V_\mathrm{I}/2$ are shown: 125 m/s for WHA-III, 175 m/s for WHA-I, II, and IV, and 225 m/s for WHA-V. Note that simulations WHA-II and V display the most uniform wave shape (both with equiaxed microstructure transverse-1), with a few fluctuations on the order of the grain diameter for $y > 80$ nm. Simulations WHA-III and IV (microstructure transverse-2) display some variations on the order of the grain diameter, as well as some smaller fluctuations. Finally, simulation WHA-I shows grain-scale fluctuations in the interior of the sample, $30 < y < 120$ μm, with significant attenuation of the wave near the lateral boundaries at $y = 0$ and $y = L$. The drop in particle velocity along the transverse boundaries for simulation WHA-I in Fig. 27 (see also Fig. 28a) could be attributed to a combination of factors, including those arising from

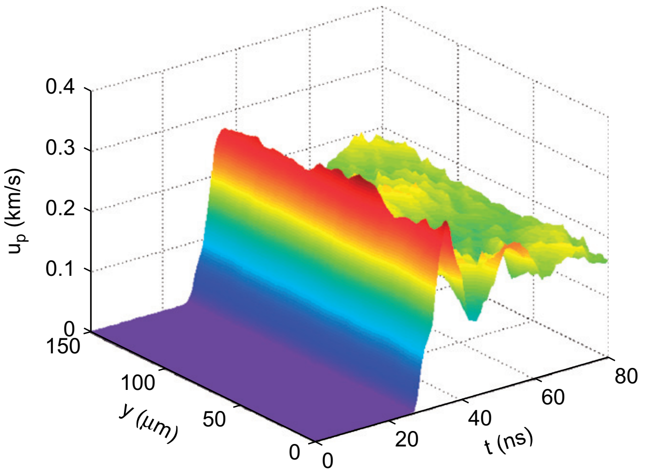

Fig. 22. Free-surface velocity history from simulation WHA-IV.

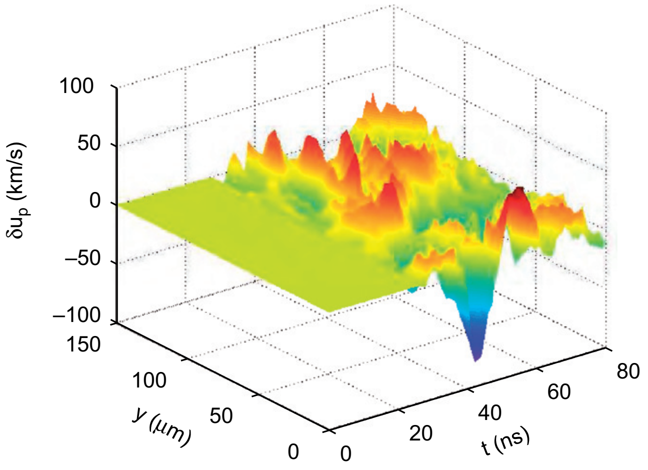

Fig. 23. Perturbations of free-surface velocity from simulation WHA-IV.

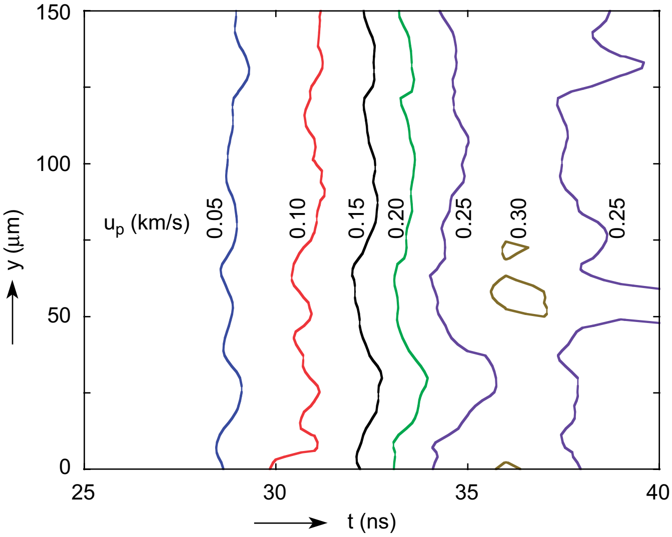

Fig. 24. Contours of constant free-surface velocity of shock front in y–t plane from simulation WHA–IV.

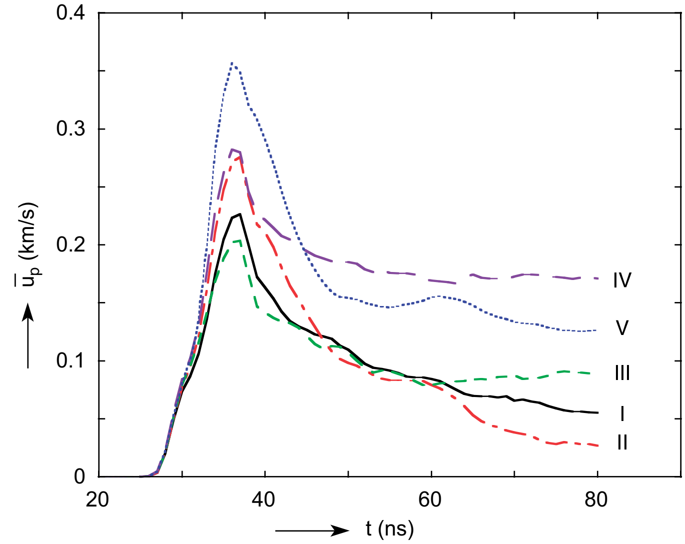

Fig. 25. Spatially averaged free-surface velocity histories for all simulations.

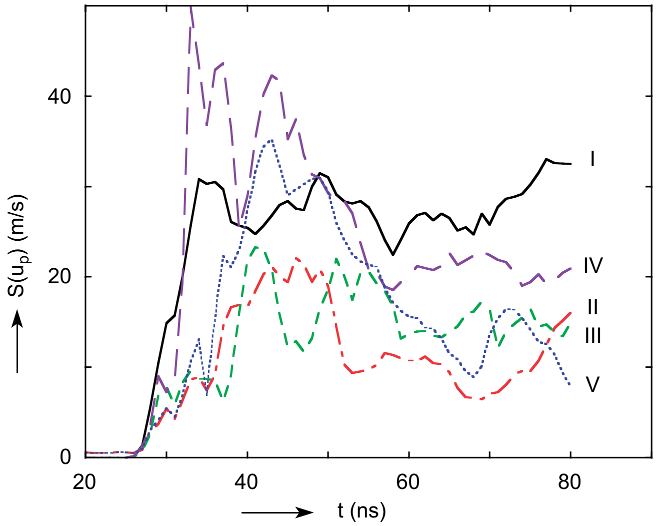

Fig. 26. Standard deviation in free-surface velocities from simulations.

inherent statistical variations in material properties related to phase distributions and lattice orientations. Significant localized plastic deformation and heating were also observed along these boundaries, which affect the stiffness and wave propagation characteristics of the material in these regions. Standard deviations, S_t, for temporal positions of the contours are 0.79, 0.18, 0.33, 0.21, and 0.14 ns for simulations WHA-I to V. The deviation for WHA-I is excessive due to the drop in velocity at the boundary. As with the experiments, the deviation of the contour decreases with impact velocity so that the ratio between S_t for 350 m/s impact (WHA-IV) and that at 250 m/s (WHA-III) is 0.65, very close to the experimental value of around 0.6. The ratio for 450 (WHA-V) and 350 m/s is somewhat higher at 0.78, but a comparison with experimental results is not possible because of the problems with experiment WHA-5. The orientation of the mesh clearly affects the roughness of the contour as the ratio for transverse-1 (WHA-II) and transverse-2 (WHA-IV) simulations is 0.86. Finally, if we estimate S_t for the central region of WHA-I, we find a value of about 0.15 ns, which would give a ratio of 0.71 for the axial and transverse-2 orientations, close to the value seen

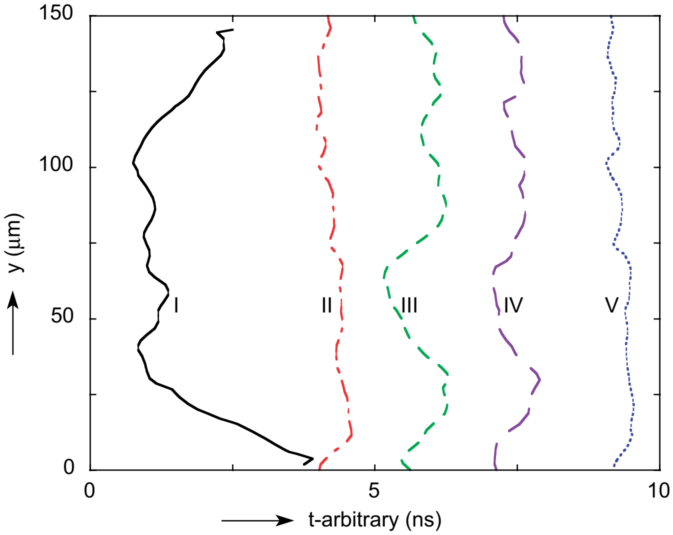

Fig. 27. Contours of constant free-surface velocity ($V_I/2$) of shock front in y–t plane for simulations WHA I–V.

experimentally. Thus, the trends for non-uniformity in simulated waves across their fronts agree with those seen experimentally.

Shown in Figs. 28 and 29 are contours of particle velocity magnitude $|\mathbf{u}_p|$ and effective stress σ^{eff} for simulations WHA-I (Fig. 28) and IV (Fig. 29), at $t = 20$ ns, when the impact wave has traversed roughly $\frac{2}{3}$ of the sample. Particle velocity vectors are also shown, superimposed on the contours of $|\mathbf{u}_p|$ and scaled in length by magnitude of local velocity. Vortices in material motion, with characteristic lengths on the order of the grain size, are apparent in the wake of the elastic–plastic stress wave. These vortices do not appear to occur preferentially within particular grains or a particular phase of the alloy, however. Heterogeneities in the wave front induced by the microstructure are also obvious. Comparing Figs. 28(a) and 29(a), the reduction in particle velocity near the lateral edges $y = 0$ and $y = L$ is apparent in the former (WHA-I). From the stress contours, W grains tend to support relatively larger effective stresses than the more ductile binder phase. Comparing Figs. 17 and 18 with 28 and 29, note that momentum conservation requires that the pressure be more uniform than the effective deviatoric stress; i.e., for the boundary conditions applied here, W grains tend to support larger deviatoric stresses than the binder does, but pressures are not preferentially higher in either phase.

5.3. *Statistics of free-surface velocity and trends in fracture*

Because the wave mechanics for the problem domain and boundary conditions of Eq. (19) do not correspond to those of a macroscopic plate impact test, the free-surface velocity profiles differ (compare Figs. 9 and 25, for example), and Eq. (23) does not apply for the simulations. However, the velocity decrement $\Delta u_{\text{fs}} = u_p^{\max} - u_p^{\min}$, where $u_p^{\max}$ is the peak particle velocity and $u_p^{\min}$ is the minimum velocity over the post-peak time interval $40\,\text{ns} \leqslant t \leqslant 80\,\text{ns}$, may provide some insight into fracture mechanisms and a means of comparison with trends in experimental spall data. Note that the larger the value of $u_p^{\min}$, the greater the residual velocity of the spalled material. Likewise, the larger the value of $u_p^{\max}$, the greater the force of the tensile release wave resisted by the material. Statistics regarding the decrement in free-surface velocity for the simulations are shown in Table 5; both Gaussian and two-parameter Weibull fits were computed. Analogous to the experimental spall statistics in Table 4, in all simulations the velocity decrements computed from the average velocity, $\Delta u_{\text{fs}}(\bar{u}_p)$, are lower than the averages $\overline{\Delta u_{\text{fs}}}$, as differences among local maxima and minima in free-surface velocities over the time history are smoothed out by averaging in the former. Simulations WHA-III and IV exhibit the lowest relative velocity decrements, which can be further explained by Figs. 19 and 20: relatively more continuously linked fracture sites are available for this microstructure with grains elongated perpendicular to the loading/unloading direction of wave propagation. From observation of the instantaneous and cumulative damage mechanisms evident in

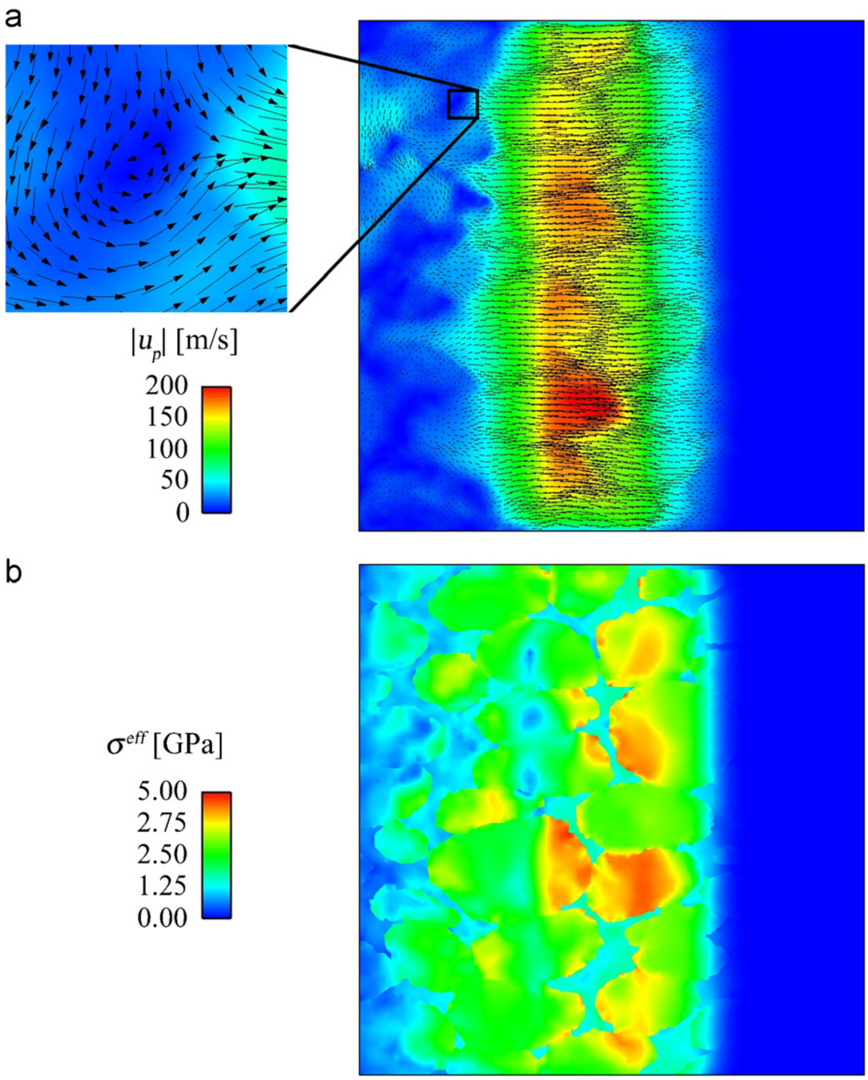

Fig. 28. (a) Particle velocity u_{p} (arrows are velocity vectors; colors indicate velocity magnitude) and (b) effective stress σ^{eff} at 20 ns for simulation WHA-I.

Figs. 19–21, the most spall-resistant microstructure at the moderate impact velocity ($V_{\mathrm{I}} = 350\,\mathrm{m/s}$) is apparently transverse-1 (WHA-II), with the highest value of $\overline{\Delta u_{\mathrm{fs}}} = 258\mathrm{m/s}$ among the five simulations. Transverse-2 is apparently the least resistant to spall fracture (WHA-IV), with the lowest value $\overline{\Delta u_{\mathrm{fs}}} = 135\,\mathrm{m/s}$ among the simulations, for the reason noted above. Standard deviations $S(\Delta u_{\mathrm{fs}})$ range from 13–18 m/s, except for simulation WHA-I. This case exhibits the largest variation in free-surface velocity drop ($S(\Delta u_{\mathrm{fs}}) = 28\,\mathrm{m/s}$), which agrees with the velocity scatter evident in Fig. 26 for that simulation. Computed Weibull moduli range from 7.82 to 18.77, somewhat higher than those in the experiments.

6. Discussion

6.1. Comparison of results: experiments and simulations

One objective of the present work is assessment of the feasibility of comparison of results from spatially resolved plate impact tests with microstructure scale plasticity and fracture simulations. Such comparisons

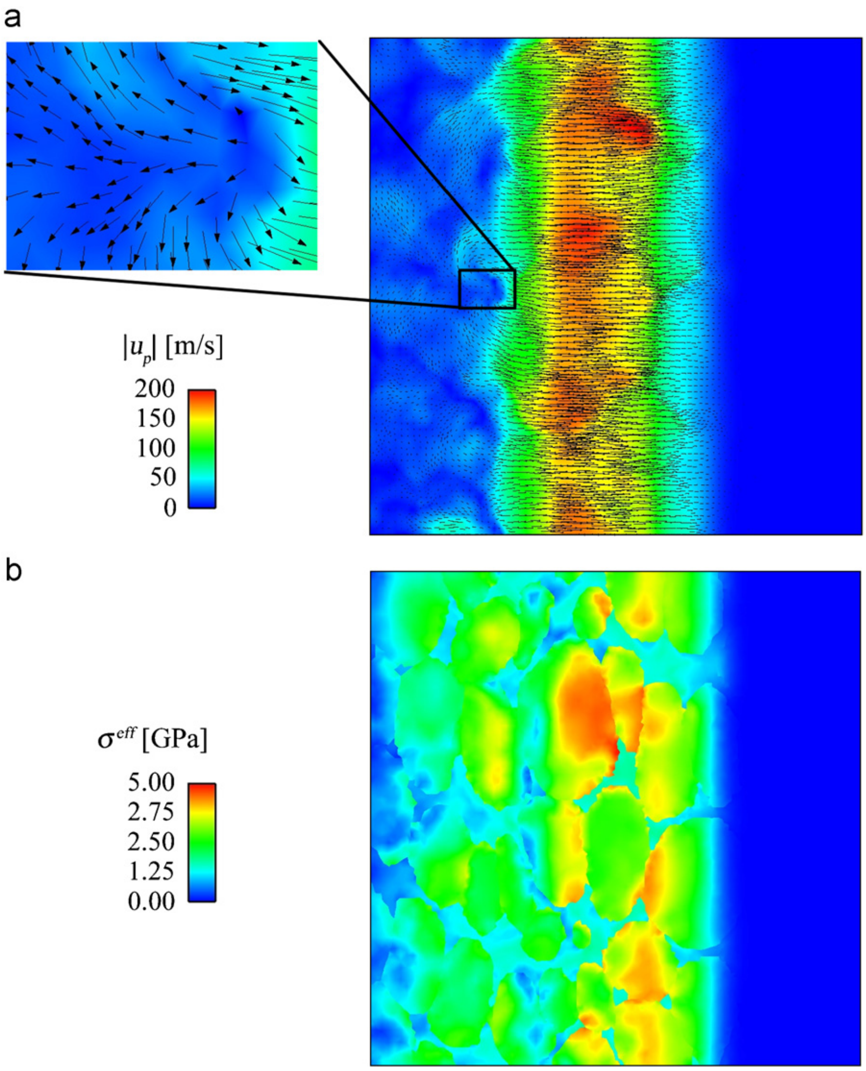

Fig. 29. (a) Particle velocity u_p (arrows are velocity vectors; colors indicate velocity magnitude) and (b) effective stress σ^eff at 20 ns for simulation WHA-IV.

Table 5
Statistical parameters for surface velocity decrements from simulations

Expt.	$\Delta u_\mathrm{fs}(\bar{u}_\mathrm{p})$ (km/s)	Normal distribution		Weibull distribution	
		$\overline{\Delta u_\mathrm{fs}}$ (km/s)	$S(\Delta u_\mathrm{fs})$ (km/s)	$\Delta u_\mathrm{fs,0}$ (km/s)	β
WHA-I	0.171	0.180	0.028	0.190	8.74
WHA-II	0.249	0.258	0.016	0.265	18.77
WHA-III	0.125	0.141	0.013	0.147	11.28
WHA-IV	0.115	0.135	0.018	0.143	7.82
WHA-VI	0.231	0.241	0.016	0.249	14.89

permit one to understand phenomena in a way not available through experiments or modeling alone and suggest means of potential improvement in the existing techniques. Some of the key findings of the current study relevant to this are as follows.

Regarding free-surface velocity profiles:

- Spatial fluctuations on the order of several or tens of grains (~0.5 mm) are observed in free surface velocity profiles collected from the experiments (Figs. 7, 8, and 11).
- Spatial fluctuations on the order of the grain size (~10–30 μm) are apparent in many of the free surface velocity profiles collected from the simulations (Figs. 22–24 and 27).
- Standard deviations in spatially resolved free surface velocity, $S(u_p)$ are typically on the order of 10 m/s for experiments (Fig. 10), and 10-30 m/s for simulations (Fig. 26).
- A significant spike is seen in the standard deviation of the free surface velocity at the time of arrival of the initial shock in the experiments, but no such spike is evident the simulations.
- Following the initial spike, the standard deviation remains relatively constant in the experiments, though most experiments show a moderate change when the particle velocity increases (the pullback signature). Some simulations show a similar behavior, but others decrease or increase noticeably, though the time scale of the simulations is significantly shorter than that of the experiments.

Regarding spall fracture:

- The experimental results indicate that the transverse orientation exhibits the lowest spall strength, as reported in Table 4. The magnitudes of differences in spall strengths for samples with different microstructures were inconsistent, however. The difference in average strengths $\bar{\sigma}_{\text{sp}}$ between WHA-1 and 3 is 0.07 GPa (both tests at 250 m/s impact velocity), whereas the difference is 0.46 GPa between WHA-2 and WHA-4 (both at 350 m/s). Similar trends apply for the Weibull parameter σ_0.
- The computations indicate that the transverse-2 microstructure exhibits the lowest spall strength, as can be ascertained from consideration of the damage mechanisms evident in Figs. 19–21 and the lowest value of free-surface velocity decrement listed in Table 5.
- Experimentally, higher velocity impacts yield a somewhat higher spall strength, $\bar{\sigma}_{\text{sp}}$, for both orientations. In contrast, the simulations exhibit a tendency to fracture more extensively when the impact velocity is increased.
- In experiments and modeling, no relationships between microstructure, impact velocity, and standard deviations of spall strength or free-surface velocity drop are readily apparent (Tables 4 and 5).
- Values of Weibull modulus β are significantly higher among the free-surface velocity decrement from the simulations (Table 5, ranging from 7.8 to 18.8) than the spall strengths from experiments (Table 4, ranging from 3.5 to 6.9).

Differences in free-surface velocity profiles arise naturally as a result of differing scales of resolution in the experiments and models. From the above observations, the simulations reflect local heterogeneity of wave propagation induced by the differences in deformations among individual grains and the softer matrix phase surrounding them, whereas the experiments detect gradients in microstructure properties among aggregates of grains, reflected in the free-surface velocity data.

The spatial resolution of the experiments is established by the capabilities of the line-VISAR instrument. The resolution along the line can be varied, but optical instrumentation limits its minimum to around 15–20 μm. However, even if the nominal resolution is 15 μm, each measurement encompasses the response of about 60 μm of material because of the procedure used for data collection and analysis. Decreasing the resolution along the line also results in a reduction in the amount of material that is being monitored by the instrument. Depending upon the dominant length scales for material behavior, monitoring a smaller amount of material may cause important behaviors to be missed. It may also affect the reliability of statistics associated with material failure.

The spatial resolution of the simulations is established by the finite element discretization. The approach here has been to use the finest FE mesh permissible within computing constraints. The elements used here are of small enough size, with typical elements on the order of 1 μm in dimension in the vicinity of grain boundaries, to resolve critical cohesive zone lengths and compute, with precision, the average material response (e.g., homogenized stress–strain behavior) as discussed in Clayton (2005a, b). However, minute aspects of fracture and the local material response are inevitably sensitive to mesh construction and the corresponding degree of resolution of microstructure features. For example, the finer the mesh, the greater the potential for a more faithful representation of the actual microstructure in the numerical reconstruction, including initial lattice orientation gradients within grains and facets of potential fracture along grain and phase boundaries. More refined grids than those used presently were prohibitively expensive from a computational standpoint, but they would enable the possibility of detection of even smaller fluctuations in free-surface velocities. Such finer grids were deemed unnecessary, since the elements used at present were small enough to detect features an order of magnitude smaller than the size of individual grains, and the grain size appeared to be the dominant feature or characteristic length reflected in the results of the simulations. To this end, averages and standard deviations of spall strength were also computed using only every other free-surface node at $X = L$, and variations in these values were negligible with those presented in Table 5, computed using all free-surface nodes. Furthermore, the element sizes used here are of comparable or smaller magnitudes than those used by others in similar investigations (Becker, 2004; Love and Batra, 2005; Zhou et al., 1994).

Substantial variability among the results from simulations is expected among different reconstructions of the material (i.e., microstructures reproduced from different regions of the material) of the present dimensions, on the order of 50 W grains. Variability is also present in physical experiments, even properties averaged over macroscopic dimensions. For example, differences in spall strengths exist among realizations in the present work and among the results of Dandekar and Weisgerber (1999). For materials undergoing catastrophic failure (i.e., crack propagation, interaction, and percolation) as occurs in spall events, a sample of large enough dimensions to act faithfully as an RVE (cf. Hill, 1963) does not exist. In other words, even for a sample of very large dimensions, variations in spall strength are expected; e.g., witness the non-negligible variations in measured spall strength (on the order of 10–15%) among macroscopic samples of the same nominal composition tested by Dandekar and Weisgerber (1999). This implies that an RVE must be significantly larger than even these plate impact samples of dimensions on the order of mm, and that failure may be controlled by a few critical, minute intrinsic flaws in the material. This does not mean the present analyses are of no scientific value, but rather indicates that all samples of the material should not behave in the same way with regards to failure/fracture. Collection of definitive statistics on variability among samples of material with similar, but not identical, microstructures (e.g., samples of material of the same global orientation cut from different locations in the KE rod) would presumably require many more experiments and simulations. However, a potential benefit of the line-VISAR technique is that variability in material properties such as spall strength due to mesostructural heterogeneity can be quantified in fewer experiments than required by a conventional point-VISAR.

In the modeling, simple hardening-minus-dynamic-recovery relationship is used (Eq. (15)) for the evolution of the slip system hardness variable $g_0^{(\alpha)}$ (Horstemeyer et al., 1999). The partitioning of $g_0^{(\alpha)}$ into a constant term $g_y^{(\alpha)}$ consisting of the effects of initial defects and lattice friction stress (Qiu et al., 2001) and an evolving hardening term is a construct used purely to illustrate the accumulation of dislocations with strain and delineate the effects of these defects versus those initially present, via (14). The present formulation for plastic slip kinetics invokes a thermal softening relationship (13) that scales the total hardness $g_0^{(\alpha)}$, the sum of initial and cumulative effects, with temperature, following the viscoplastic models of Lee et al. (1999) and Klopp et al. (1985). No physical basis is attached to the reference strain rate $\dot{\gamma}_0$, treated here as an arbitrary constant, following Hutchinson (1976). The present approach was found to adequately address the rate- and temperature-dependent stress–strain behavior for both phases over the range of loading rates for which the models were calibrated, from quasi-static to those achievable via Hopkinson bar, the latter on the order of $10^4\,\mathrm{s}^{-1}$ (Clayton, 2005a). However, refinements to the present formulation are possible that would perhaps provide a more realistic description of the physics of thermally activated dislocation motion. For example, rather than scaling all slip resistance mechanisms uniformly via a thermal softening relation such as Eq. (13), one could enable the hardening and recovery terms A and B in (15) to more realistically depend on temperature in an independent manner, e.g., $A \propto \exp(A_1/\theta)$ following (Bammann et al., 1993), where A_1 is a constant related to the activation energy. Likewise, the friction stress and initial dislocation density contributions to $g_y^{(\alpha)}$ may not scale in the same way with temperature as imposed by the present model. Additionally, as remarked in Balasubramanian and Anand (2002), the reference shearing rate could be assigned a physical meaning following a Boltzmann relation of the form $\dot{\gamma}_0 \propto \exp(Q/k_{\mathrm{B}}\theta)$, with Q the activation energy and k_B Boltzmann's constant. While the hardening-minus-recovery format (15) does lead to a saturation in flow stress at sufficient strain levels, a relation with the saturation value of flow stress based explicitly on temperature and strain rate (Kocks et al., 1975) may be more meaningful for describing dislocation kinetics under conditions explored numerically here. With increasing model refinement, however, additional experiments or assumptions will be necessary in order to calibrate all parameters uniquely.

During the present simulations, a range of inelastic strain rates was observed, with maximum rates on the order of $10^7\,s^{-1}$ attained at some time instants during propagation of plastic waves. The largest strains and strain rates were concentrated in the binder phase. The plasticity models were calibrated (Clayton, 2005a) to static and dynamic data up to the $10^4\,s^{-1}$ range (the latter obtained via Hopkinson bar testing in compression and shear), thus encompassing only partially the rates achieved during the impact simulations. A similar approach was followed by Becker (2004), who extrapolated the available data at intermediate strain rates to model the shock response of polycrystalline tantalum using crystal plasticity theory. Macroscopic viscoplastic models are also typically extrapolated to address very high strain rates within shear bands (Batra and Wilson, 1998) and early stages of pressure–shear experiments (Zhou et al., 1994), for which model calibration data at very high strain rates in excess of $10^6\,s^{-1}$ is unavailable. The difficulty arises from the unavailability of physical experiments supplying homogeneous stress–strain behavior at such high rates. In fact, one initial objective of the present investigation was suggestion of improvements in plasticity models at high rates since these strain rates are thought to occur in the plate impact tests, albeit in an inhomogeneous manner. However, such an effort was found overly difficult due to differences in scales of resolution inhibiting comparisons of model and experiment, as discussed above, and uncertainty over which of many model features should be adjusted in order to match the output from the line-VISAR. It is conceivable that in the near future, molecular dynamics (Horstemeyer et al., 2001; Moriarty et al., 2002) simulations may provide insight into the response at such high rates, since such methods are well-suited to very short time scales and very large strain rates.

The pressure–shear impact data of Zhou and coworkers (Zhou, 1993; Zhou and Clifton, 1997; Zhou et al., 1994), who observed nominal shear strain rates in excess of $10^5\,s^{-1}$ under large compressive stress, offers the potential for some improvement in the present plasticity model and choice of parameters. Zhou et al. (1994) calibrated an isotropic viscoplastic model to this data and found close agreement between model predictions and experimental shear stress–strain curves during later stages of the test ($t > 100\,ns$), when wave reverberations had decayed and the specimen experienced a nearly uniform state of shear stress. However, Zhou et al. (1994) noted that discrepancies arose between experiment and model predictions at early stages of the impact event, attributed in their paper to inadequacy of the constitutive model at the high initial shearing rates as well as possible experimental difficulties. It is precisely this regime of elastic–plastic wave propagation ($t < 100\,ns$) that is of interest in the present simulations, albeit for normal as opposed to inclined impact conditions. The present crystal plasticity model could conceivably be calibrated to the pressure–shear impact data of Zhou (1993) on pure W and the matrix alloy to better address the response of these materials at rates up to $2 \times 10^5\,s^{-1}$. Calibration to such data would presumably require consideration of the crystal structure (thin films, several grains thick) and texture, following the approach of Duprey and Clifton (2000), for example, who modeled with distinct finite elements and crystal plasticity theory, individual grains of tantalum under pressure–shear impact. Such a rigorous approach may be contrasted to the much simpler Taylor-type approximation typically used to calibrate such models to uniaxial and Hopkinson bar data. It is thought that specimen preparation may affect the properties, since Zhou (1993) demonstrated a dependence of the dynamic flow stress of WHA on the cross rolling process used to fabricate the pressure–shear samples. It is also possible that the large compressive pressure pulse may affect the lattice structure and induce defects, thereby affecting the flow stress measured at later times during the experiment. Such effects would implicitly be included in the parameters determined from calibration to the shear stress-strain data provided by the test. Perhaps the best approach to calibrate the plasticity models over the full range of strain rates attained during plate impact testing would be to conduct independent experiments and calibration simulations of specimens of single phase composition (i.e., pure W or pure matrix), uniform initial texture, and with the same spatial dimensions and impact speeds used for both experiments and simulations. However, some uncertainty would still exist in the response of the matrix phase, which in the WHA resides in thin layers between W grains and as a result may exhibit different properties than the pure matrix alloy whose typical grain size tends to exceed that of the W grains.

Millett et al. (2007) performed plate impact tests on pure polycrystalline W and compared the observed behavior with WHA reported from several sources. The HEL values of pure W and WHA materials were found to be similar. In pure W, a mechanism of brittle micro-cracking induced by the compressive pulse was suggested, following an observation of progressively reduced shear strength behind the shock front.

Finally, a discrepancy between experiments and simulations exists due to the 2D nature of the simulations. Real materials have complex modes of deformation and failure, particularly with regards to evolution of fracture surfaces that cannot be faithfully captured by 2D simulations. Future increases in computing power will make comparably detailed numerical studies of plasticity and fracture at the grain level feasible in three dimensions.

6.2. *Material behavior*

Mescheryakov and coworkers (Mescheryakov, 2003; Mescheryakov et al., 2004) developed a multiscale descriptive framework for describing effects of micro- or meso-structures on wave propagation in solids under impact loading. In their framework, dispersions of particle velocities are analyzed at three scales of increasing characteristic length: mesolevel-1, mesolevel-2, and macroscale. Instability under shock compression is characterized by exhaustion of dissipative mechanisms and attainment of a maximum value of dispersion at the finest length scale, mesolevel-1. Subsequently, dispersion at mesolevel-2 increases as regions of localized shear or damage interact at a larger length scale, culminating in final failure or percolation of the sample (e.g., macroscopic spall failure). In this framework, the simulations indicate dispersion at the grain scale, corresponding to Mescheryakov's mesolevel-1, while the experiments are indicative of dispersion at a larger length scale not measurable in the simulations, mesolevel-2.

Case and Horie (2007) recently used a DEM to model impact and shock wave propagation in polycrystalline copper at the mesostructure scale, with a level of resolution comparable to that used in the present work, though these authors did not attempt to model spall fracture explicitly. Case and Horie (2007) found that the particle velocity dispersion (i.e., standard deviation $S(u_{\mathrm{p}})$) at the shock front depends upon the impact stress, in agreement with the trends from the current experiments and simulations. Also, in another DEM study of copper, Yano and Horie (1999) noted vortices in material flow in the wake of the shock pulse, similar in scale and appearance to those presented here in Figs. 28 and 29. In that work, non-uniform tensile stresses were observed where waves interact, indicating that a spall strength distribution can be obtained even with constant material strength. Such is also the case in the present study, where a distribution of spall strengths was found for a heterogeneous crystalline material with uniform cohesive strength. Finally, Case and Horie (2007) noted peaks in the particle velocity dispersion of about twice the magnitude of that found at later, steady-state times in the impact events. Such spikes were observed in the experiments, as shown in Fig. 10, but were absent in our numerical results, Fig. 26. According to Mescheryakov and Astroshenko (1992), such a peak should occur at the midway point of the plastic wave rise, when effects of mesoscopic rotations of material manifest most strongly. The reason for the absence of such a peak in the numerical results is not obvious at present. One possibility is that the kinetic equations for plasticity, with strain-rate dependent hardening in Eqs. (12)–(15), cause some smoothing of the plastic wave, as different plasticity kinetics were used in the study of Case and Horie (2007).

Though mild crystallographic textures indicative of extrusion along the axial direction existed, specific effects of lattice orientation could not be delineated among particular experiments or simulations. Only slight differences in average compliance among experiments with different initial microstructures were observed (Table 1), and neither experiments nor simulations clarified whether such differences were attributed to initial lattice orientation, grain morphology (i.e., elongated versus equiaxed grains with respect to loading axis), spatial distribution of the binder phase, or other factors. Similar ambiguity exists as to how individual aspects of the microstructure, including textures and grain shapes, may affect wave arrival times and pull-back velocities. One may speculate that fewer distinct lattice orientations along the axial direction among the W grains may reduce the dispersion in free-surface velocity profiles in axial samples relative to transverse samples, since the contours of constant free-surface velocity are more jagged in transverse samples than axial samples in Fig. 11. This effect could be attributed to fewer distinct orientations in axial samples that tend slightly towards a $\langle 1\,1\,0 \rangle$ texture, or fewer W grains across the thickness of the sample since the grains are elongated in the axial direction. However, in contrast, simulations of the microstructure transverse-1 exhibited the fewest fluctuations in free-surface velocity (Figs. 26 and 27). One may just as easily speculate that the larger number of (equiaxed as opposed to elongated) grains through the thickness of the transversely oriented samples may smooth out the fluctuations induced by individual crystals of various initial orientations. Clearly, more extensive investigations, in which sample-to-sample variations in microstructure are restricted to texture alone, are needed to fully elucidate possible effects of lattice orientation on the response of WHA.

As remarked above, the transverse microstructure exhibits the lowest average spall strength in the experiments. Note that this microstructure presents a relatively large area per unit volume of grain boundary surfaces perpendicular to the loading direction, in contrast to the axial orientation, whose grains are elongated along the axis of impact (Fig. 1(a)). Since the weakest link in the material is expected to control initiation of failure, the transverse orientation should have average spall strengths that are lower than those of the axial orientation. For example, failure of a typically larger grain boundary facet elongated perpendicular to the loading direction would present a larger starter crack for eventual catastrophic fracture than would failure of a typically smaller grain boundary facet in a microstructure with equiaxed or shortened grains aligned perpendicular to the loading direction. In the simulations, the transverse-2 microstructure possesses the lowest strength. The reason for this is clear from grain and phase boundary arrangements and examining the fracture sites in the simulations of Figs. 19 and 20. Since the primary fracture criterion in the simulations follows from the maximum resolved normal stress acting on grain or phase boundaries (Eqs. (16) and (17) and $\hat{s}_0$ of Table 2), those microstructures presenting the greatest number of contiguous fracture sites oriented perpendicular to the impact direction tend to fail most readily. Note that simulations II and V, with the transverse-1 microstructure, exhibit the highest apparent resistance to spall fracture. Transversely oriented samples include both transverse-1 and transverse-2 orientations, depending upon how one views the sample. In the simulations, these microstructures are not equivalent, however. Even though both may have comparable grain boundary area per unit volume, microstructure transverse-2 exhibits more grain boundary facets oriented most nearly parallel to the loading axis. Correspondingly, the lower average value of free surface velocity decrement (WHA IV, Table 5) seems to reflect a tendency for damage accumulation evident in Fig. 21.

The experiments indicate that higher velocity impacts produce a higher spall strength, $\bar{\sigma}_{\mathrm{sp}}$. This suggests that the regions where failure occurs (e.g., W-matrix interfaces and W–W grain boundaries) are preconditioned to a more durable state by the initial compressive pulse. Such behavior has been observed previously in other brittle materials (Dandekar, 2004). Physically, this phenomenon could correspond to closure of microvoids or elimination of deleterious effects of other defects caused by impurities at the boundaries. On the other hand, the simulations predict somewhat lower spall strength when the impact velocity is increased, despite the increase in fracture toughness with temperature provided by Eq. (16). The correct behavior could be reflected in future simulations by incorporating cohesive traction laws dependent upon the stress history of the local material.

It is suggested here that initiation of spall fracture may be controlled by grain and phase boundaries, in agreement with experimental observations of (Weerasooriya, 2003). However, crack propagation and macroscopic spall behavior are thought to also require substantial grain cleavage: once a sufficiently large, a micro-crack initiated along grain/phase boundaries will then propagate fully across the specimen, irrespective of the underlying microstructure. Post mortem inspection of fully fractured (i.e., spalled) specimens would then likely indicate both intergranular and cleavage mechanisms (Bless and Chau, 2006). The simulations (Figs. 19 and 20) also demonstrate that for complete fracture to occur, cleavage must take place, since insufficient fracture sites for purely intergranular fracture likely exist to allow for crack propagation across a sample of dimensions of several hundred microns or larger. This assertion was also made in Clayton (2005a) in the context of dynamic tensile loading. Grain and phase boundaries should also exhibit a distribution of strengths; for example, Weerasooriya et al. (1994) suggested that W–W boundaries are intrinsically weaker than W-matrix boundaries. Clayton (2005a) investigated the effect of variable ratios of grain and phase boundary strengths on uniaxial tensile failure. The role of such variable grain boundary strengths on spall fracture statistics remains to be investigated in future modeling work. Based on the current results, it is apparent that the variability in spall statistics observed experimentally is due both to the heterogeneous local strengths and flaw distributions and to the multiphase polycrystalline microstructure of the material.

6.3. Future work

In the future, multiple realizations of the same experiments (i.e., same impact velocity and sample orientation) should be conducted to quantify sample-to-sample variability in wave propagation and spall properties. Analogously, additional simulations should be performed with microstructures of similar global characteristics (e.g., equiaxed vs. extruded grains) but different local characteristics (e.g., individual grain shapes and orientations). Such simulations would provide additional support for the hypothesized dependence of spall strength on orientation, for example.

7. Conclusions

A combined experimental–computational study, accounting for the effects of microstructure on wave propagation and spall fracture, was conducted on a tungsten heavy alloy subjected to normal plate impact loading. In the experiments, a line-VISAR system enabled the resolution of particle velocity profiles at the scale of tens of microns. In the simulations, crystal plasticity theory coupled with a cohesive zone model for intergranular and interphase fracture enabled the resolution of local thermomechanical response of the material at the micron scale.

The large volume of experimental data collected, and corresponding analysis of this data, provide a detailed description of the material's high-rate behavior and mechanical properties. Specifically, for WHA microstructures of different microstructure orientations, the following information was obtained: spatially resolved free-surface velocity profiles, HELs, spall strengths, and spall statistics. While the bulk HEL values and average spall strengths obtained here are comparable with results obtained from previous point-VISAR experiments (Dandekar and Weisgerber, 1999), the detailed statistical aspects of wave propagation and fracture have heretofore been unavailable. Such statistics may support future macroscopic modeling of dynamic deformation and failure of the WHA material. For example, the Weibull modulus may be used to provide initial conditions for simulations employing spatially variable failure properties (Brannon et al., 2007; Goto et al., 2007; Schraml et al., 2005; Zhou and Molinari, 2004).

From the simulations, local behavior not accessible in the experiments was observed. Plastic strain accumulation and dislocation activity tended to be greatest in the more ductile matrix phase of the WHA material, whereas larger effective deviatoric stresses were supported by the W grains. Heterogeneous impact wave propagation and vortices in material motion behind the plastic wave were found to occur at the scale of individual grains. Local fracture morphologies were also observed, with details of micro-cracking dependent upon initial microstructure and impact velocity. Effects of microstructure orientation and impact velocity on aspects of spall fracture described here have not, to our knowledge, been quantified in previous modeling studies of WHA. In the simulations, differences in spall behavior arise strictly as a result of the dual phase granular microstructure, since a uniform value was used for the strength of the cohesive zone elements. One likely reason that the velocity statistics in the simulations differ from those observed in the experiments is that the local variations associated with spall strength in the experiments may be attributed to microstructural heterogeneities not resolved by the model (e.g., defects or flaws within grains) and to the presence of grain and phase boundary strength distributions.

In both experiments and simulations, similar effects of microstructure on overall fracture resistance were observed. Grain boundaries seemed to dominate fracture initiation in either case, with microstructures presenting the most area per unit volume perpendicular to loading direction exhibiting the least strength. Differing scales of resolution between model (fine resolution, but limited to small sample sizes) and experiment (larger sample, but less refined resolution) partially inhibited direct comparison of results. For example, variations in free surface velocity profiles on the order of grain size were observed in the simulations, while variations on the order of multiple grains were observed in the experiments. Despite the different scales involved, though, the dispersion of the initial shocks was found to scale in nearly the same way with velocity and orientation for experiments and simulations.

The present study has suggested methods for improved concurrent experimental and modeling efforts in the future. In the experiments, a still unresolved issue is the effect of sample thickness on heterogeneous wave propagation. For example, the post-spall wave profiles include not only the effects of the heterogeneous fracture pattern, but also the effects of wave propagation through undamaged but heterogeneous material between the spall plane and the free surface. More refined techniques enabling in situ study of the wave propagation and spall behavior on the scale of individual grains or even smaller (e.g. micron scale) would also be instructive. The present simulations permit correlation of local fracture behavior and microstructure effects to the simulated free-surface velocity profiles. Incorporation of grain cleavage models for this particular alloy, and improvements in computational methods for dynamic crystal plasticity and cohesive fracture to address much larger sample sizes, with dimensions on the order of millimeters and at time scales on the order of microseconds, would enable more useful, direct comparison with plate impact experiments of the same dimensions.

Acknowledgments

The authors would like to thank Wayne Trott, Jaime Castañeda, and the STAR team for performing the line-VISAR experiments. We would also like to thank Tony Rollett of Carnegie-Mellon University for the EBSD results as well as Todd Bjerke and William Edmanson (both of ARL) for obtaining the material specimens. Work at Sandia was supported through the Joint DoD/DOE Munitions Technology Development Program. Sandia is a multiprogram laboratory operated by Sandia Corporation, a Lockheed Martin Company, for the United States Department of Energy's National Nuclear Security Administration under Contract DE-AC04-94AL85000. J.D.C. acknowledges support from the US Army Research Laboratory (ARL).

References

Antoun, T.H., Seaman, L., Curran, D.R., Kanel, G.I., Razorenov, S.V., Utkin, A.V., 2003. Spall Fracture. Springer-Verlag, New York.

Argon, A.S., Maloof, S.R., 1966. Plastic deformation of tungsten crystals at low temperatures. Acta Metall. 14, 1449–1462.

Asaro, R.J., 1983. Crystal plasticity. J. Appl. Mech. 50, 921–934.

Asay, J.R., Barker, L.M., 1974. Interferometric measurement of shock-induced internal particle velocity and spatial variations of particle velocity. J. Appl. Phys. 45, 2540–2546.

Asay, J.R., Chhabildas, L.C., 2003. Paradigms and challenges in shock wave research. In: Horie, Y., Davison, L., Thadhani, N.N. (Eds.), High-pressure Shock Compression of Solids VI: Old Paradigms and New Challenges. Springer, New York, pp. 57–119.

Baer, M.R., Trott, W.M., 2004. Mesoscale studies of shock loaded tin sphere lattices. In: Furnish, M.D., Gupta, Y.M., Forbes, J.W. (Eds.), Shock Compression of Condensed Matter. American Institute of Physics, New York, pp. 517–520.

Baer, M.R., Trott, W.M., 2005. Theoretical and experimental mesoscale studies of impact-loaded granular explosive and simulant materials. In: Proceedings of the 12th International Symposium on Detonation. Office of Naval Research, 333-05-2, pp. 939–948.

Balasubramanian, S., Anand, L., 2002. Plasticity of initially textured hexagonal polycrystals at high homologous temperatures: application to titanium. Acta Mater. 50, 133–148.

Bammann, D.J., Chiesa, M.L., Horstemeyer, M.F., Weingarten, L.I., 1993. Failure in ductile metals using finite element methods. In: Jones, N., Weirzbicki, T. (Eds.), Structural Crashworthiness and Failure. Elsevier, New York, pp. 1–53.

Baoping, Z., Chao, Y., Yingming, X., Chunlan, J., 1994. Responsive behaviour of 93 wt% tungsten alloy under intense shock loading. In: Zhemin, Z., Quinming, T. (Eds.), Proceedings of the IUTAM Symposium on Impact Dynamics. Peking University Press, pp. 283–297.

Barker, L.M., 2000. The development of the VISAR, and its use in shock compression science. In: Furnish, M.D., Chhabildas, L.C., Hixson, R.S. (Eds.), Shock Compression of Condensed Matter. American Institute of Physics, New York, pp. 11–17.

Batra, R.C., Wilson, N.M., 1998. Adiabatic shear bands in plane strain deformations of a WHA. Int.J. Plasticity 14, 43–60.

Baumung, K., Singer, J., Razorenov, S.V., Utkin, A.V., 1996. Hydrodynamic proton beam-target interaction experiments using an improved line-imaging velocimeter. In: Schmidt, S.C., Tao, W.C. (Eds.), Shock Compression of Condensed Matter. American Institute of Physics, New York, pp. 1015–1018.

Becker, R., 2004. Effects of crystal plasticity on materials loaded at high pressures and strain rates. Int. J. Plasticity 20, 1983–2006.

Bless, S., Chau, R., 2006. Tensile failure of tungsten rods. In: Furnish, M.D., Elert, M., Russell, T.P., White, C.T. (Eds.), Shock Compression of Condensed Matter. American Institute of Physics, New York, pp. 603–606.

Bloomquist, D.D., Sheffield, S.A., 1983. Optically recording interferometer for velocity measurements with subnanosecond resolution. J. Appl, Phys. 54, 1717–1722.

Brannon, P.J., Konrad, C.H., Morris, R.W., Jones, E.D., Asay, J.R., 1983. Studies of the spectral and spatial characteristics of shock-induced luminescence from X-cut quartz. J. Appl. Phys. 54, 6381–6474.

Brannon, R.M., Strack, O.E., Lee, M.Y., 2007. Spatial statistics of material strength to address mesh dependency of conventional damage models. Part I: theory and experiments, in preparation.

Bury, K.V., 1975. Statistical Models in Applied Science. Wiley, New York (Chapter 12).

Case, S., Horie, Y., 2007. Discrete element simulation of shock wave propagation in polycrystals. J. Mech. Phys. of Solids 55, 589–614.

Chhabildas, L.C., Trott, W.M., Reinhart, W.D., Cogar, J.R., Mann, G.A., 2002. Incipient spall studies in tantalum–microstructural effects. In: Furnish, M.D., Thadhani, N.N., Horie, Y. (Eds.), Shock Compression of Condensed Matter. American Institute of Physics, New York, pp. 483–486.

Clayton, J.D., 2005a. Dynamic plasticity and fracture in high density polycrystals: constitutive modeling and numerical simulation. J. Mech. Phys. Solids 53, 261–301.

Clayton, J.D., 2005b. Modeling dynamic plasticity and spall fracture in high density polycrystalline alloys. Int. J. Solids Structures 42, 4613–4640.

Clayton, J.D., 2006a. Continuum multiscale modeling of finite deformation plasticity and anisotropic damage in polycrystals. Theor. Appl. Fract. Mech. 45, 163–185.

Clayton, J.D., 2006b. Plasticity and spall in high density polycrystals: modeling and simulation. In: Furnish, M.D., Elert, M., Russell, T.P., White, C.T. (Eds.), Shock Compression of Condensed Matter. American Institute of Physics, New York, pp. 311–314.

Dandekar, D.P., 2004. Spall strength of silicon carbide under normal and simultaneous compression-shear shock wave loading. Int. J. Appl. Ceram. Technol. 1, 261–268.

Dandekar, D.P., Weisgerber, W.J., 1999. Shock response of a heavy tungsten alloy. Int. J. Plasticity 15, 1291–1309.

Duprey, R.C., Clifton, R.J., 2000. Pressure–shear response of thin tantalum films. In: Furnish, M.D., Chhabildas, L.C., Hixson, R.S. (Eds.), Shock Compression of Condensed Matter. AIP Press, New York, pp. 447–450.

Espinosa, H.D., Zavattieri, P.D., 2003a. A grain level model for the study of failure initiation and evolution in polycrystalline brittle materials. Part I: theory and numerical implementation. Mech. Mater. 35, 333–364.

Espinosa, H.D., Zavattieri, P.D., 2003b. A grain level model for the study of failure initiation and evolution in polycrystalline brittle materials. Part II: numerical examples. Mech. Mater. 35, 365–394.

Furnish, M.D., Trott, W.M., Mason, J., Podsednik, J., Reinhart, W.D., Hall, C.A., 2004. Assessing mesoscale material response via high-resolution line-imaging VISAR. In: Furnish, M.D., Gupta, Y.M., Forbes, J.W. (Eds.), Shock Compression of Condensed Matter. American Institute of Physics, New York, pp. 1159–1162.

Furnish, M.D., Reinhart, W.D., Trott, W.M., Chhabildas, L.C., Vogler, T.J., 2006. Variability in dynamic properties of tantalum: spall, Hugoniot elastic limit, and attenuation. In: Furnish, M.D., Elert, M., Russell, T.P., White, C.T. (Eds.), Shock Compression of Condensed Matter. American Institute of Physics, New York, pp. 615–618.

Goto, D.M., Orzechowski, T., Becker, R., 2007. Personal communication.

Gumbsch, P., Riedle, J., Hartmaier, A., Fischmeister, H.F., 1998. Controlling factors for brittle-to-ductile transition in tungsten single crystals. Science 282, 1293–1295.

Hill, R., 1963. Elastic properties of reinforced solids: some theoretical principles. J. Mech. Phys. Solids 11, 357–372.

Hirth, J.P., Lothe, J., 1982. Theory of Dislocations. Krieger, Malabar, FL.

Horstemeyer, M.F., McDowell, D.L., McGinty, R.D., 1999. Design of experiments for constitutive model selection: application to polycrystal elastoviscoplasticity. Modelling Simulation Mat. Sci. Eng. 7, 253–273.

Horstemeyer, M.F., Baskes, M.I., Plimpton, S.J., 2001. Computational nanoscale plasticity simulations using embedded atom potentials. Theor. Appl. Fract. Mech. 37, 49–98.

Hutchinson, J.W., 1976. Bounds and self-consistent estimates for creep in polycrystalline materials. Proc. R. Soc. London A 348, 101–127.

Johnson, G.R., Stryk, R.A., Beissel, S.R., 2001. User instructions for the 2001 version of the EPIC code. Alliant Techsystems, Hopkins, MN. (Distribution authorized to US government agencies and their contractors only.)

Klopp, R.W., Clifton, R.J., Shawki, T.G., 1985. Pressure–shear impact and the dynamic viscoplastic response of metals. Mech. Mater. 4, 375–385.

Kocks, U.F., Argon, A.S., Ashby, M.F., 1975. Thermodynamics and kinetics of slip. Prog. Mater. Sci. 19, 1–281.

Kocks, U.F., Tomé, C.N., Wenk, H.-R., 1998. Texture and Anisotropy: Preferred Orientations in Polycrystals and their Effect on Material Properties. Cambridge University Press, Cambridge, UK.

Lee, Y.J., Subhash, G., Ravichandran, G., 1999. Constitutive modeling of body-centered-cubic (BCC) polycrystals. Int. J. Plasticity 15, 625–645.

Love, B.M., Batra, R.C., 2005. Determination of effective thermomechanical parameters of a mixture of two elastothermoviscoplastic constituents. Int. J. Plasticity 22, 1026–1061.

Magness, L.S., 1994. High strain rate deformation behaviors of kinetic energy penetrator materials during ballistic impact. Mech. Mat. 17, 147–154.

Margetson, J., Sherwood, P.J., 1979. Statistical analysis of the brittle fracture of sintered tungsten. J. Mat. Sci. 14, 2575–2580.

McMillan, C.F., Goosman, D.R., Parker, N.L., Steinmetz, L.L., Chau, H.H., Huen, T., Whipkey, R.K., Perry, S.J., 1988. Velocimetry of fast surfaces using Fabry–Perot interferometry. Rev. Sci. Instrum. 59, 1–20.

Mescheryakov, Y.I., 2003. Meso-macro energy exchange in shock deformed and fractured solids. In: Horie, Y., Davison, L., Thadhani, N.N. (Eds.), High-Pressure Shock Compression of Solids VI: Old Paradigms and New Challenges. Springer, New York, pp. 169–213.

Mescheryakov, Y.I., Atroshenko, S.A., 1992. Multiscale rotations in dynamically deformed solids. Int. J. Solids Struct. 29, 2761–2778.

Mescheryakov, Y.I., Divakov, A.K., N.I., Z., 2004. Shock-induced structural transitions and dynamic strength of solids. Int. J. Solids Struct. 41, 2349–2362.

Meyers, M.A., Carvalho, M.S., 1976. Shock-front irregularities in polycrystalline metals. Mater. Sci Eng 24, 131–135.

Millett, J.C.F., Bourne, N.K., Rosenberg, Z., Field, J.E., 1999. Shear strength measurements in a tungsten alloy during shock loading. J. Appl. Phys. 86, 6707–6709.

Millett, J.C.F., Gray, G.T., Bourne, N.K., 2007. Measurement of the shear strength of pure tungsten during one-dimensional shock loading. J. Appl. Phys. 101, 033520.

Moriarty, J.A., Belak, J.F., Rudd, R.E., Soderlind, P., Streitz, F.H., Yang, L.H., 2002. Quantum-based atomistic simulation of materials properties in transition metals. J. Phys. Condens. Matter 14, 2825–2857.

Nemat-Nasser, S., Okinaka, T., Ni, L., 1998. A physically-based constitutive model for BCC crystals with application to polycrystalline tantalum. J. Mech. Phys. Solids 46, 1009–1038.

Qiu, X., Huang, Y., Nix, W.D., Hwang, K.C., Gao, H., 2001. Effect of intrinsic lattice resistance in strain gradient plasticity. Acta Mater. 49, 3949–3958.

Ramesh, K.T., Coates, R.S., 1992. Microstructural influences on the dynamic response of tungsten heavy alloys. Metall. Trans. 23A, 2625–2630.

Roundy, D., Krenn, C.R., Cohen, M.L., Morris, J.W., 2001. The ideal strength of tungsten. Philos. Mag. A–Phys. Condens. Matter. Struct. Defects Mech. Prop. 81, 1725–1747.

Ruoff, A.L., Rodriguez, C.O., Christensen, N.E., 1998. Elastic moduli of tungsten to 15 Mbar, phase transition to 6.5 Mbar, and rheology to 6 Mbar. Phys. Rev. B 58, 2998–3002.

Schoenfeld, S.E., 1998. Dynamic behavior of polycrystalline tantalum. Int. J. Plasticity 14, 871–890.

Schoenfeld, S.E., Kad, B.K., 2002. Texture effects on shear response in Ti–6Al–4V plates. Int. J. Plasticity 18, 461–486.

Schraml, S.J., Meyer, H.W., Kleponis, D.S., Kimsey, K.D., 2005. Simulating the formation and evolution of behind armor debris fields. In: Proceedings 2005 DoD High Performance Computing Users Group Conference.

Subhash, G., Lee, Y.J., Ravichandran, G., 1994. Plastic deformation of CVD textured tungsten–I. Constitutive response. Acta Metall. Mater. 42, 319–330.

Trott, W.M., Knudson, M.D., Chhabildas, L.C., Asay, J.R., 2000. Measurements of spatially resolved velocity variations in shock compressed heterogeneous materials using a line-imaging velocity interferometer. In: Furnish, M.D., Chhabildas, L.C., Hixson, R.S. (Eds.), Shock Compression of Condensed Matter. American Institute of Physics, New York, pp. 993–998.

Trott, W.M., Castañeda, J.N., O'Hare, J.J., Knudson, M.D., Chhabildas, L.C., Baer, M.R., Asay, J.R., 2001. Examination of the mesoscopic scale response of shock compressed heterogeneous materials using a line-imaging velocity interferometer. In: Staudhammer, K.P., Murr, L.E., Meyers, M.A. (Eds.), Fundamental Issues and Applications of Shock-Wave and High-Strain-Rate Phenomena. Elsevier, Amsterdam, pp. 647–654.

Trott, W.M., Chhabildas, L.C., Baer, M.R., Castañeda, J.N., 2002. Investigation of dispersive waves in low-density sugar and HMX using line-imaging velocity interferometry. In: Furnish, M.D., Thadhani, N.N., Horie, Y. (Eds.), Shock Compression of Condensed Matter. American Institute of Physics, New York, pp. 845–848.

Trott, W.M., Baer, M.R., Castañeda, J.N., Chhabildas, L.C., Asay, J.R., 2007a. Investigation of the mesoscopic scale response of low-density pressings of granular sugar under impact. J. Appl. Phys. 101, 024917.

Trott, W.M., Baer, M.R., Castañeda, J.N., Tappan, A.S., Stuecker, J.N., Cesarano, J., 2007b. Shock-induced reaction in a nitromethane-impregnated geometrically regular sample configuration. In: Proceedings of the 13th International Detonation Symposium, in press.

Vogler, T.J., Reinhart, W.D., Chhabildas, L.C., 2004. Dynamic behavior of boron carbide. J. Appl. Phys. 95, 4173–4183.

Weerasooriya, T., 2003. Deformation and failure behavior of a tungsten heavy alloy under tensile loading at different strain rates. In: Proceedings of the SEM Annual Conference on Experimental Mechanics.

Weerasooriya, T., Beaulieu, P.A., 1993. Effects of strain rate on the deformation and failure behavior of 93W–5Ni–2Fe under shear loading. Mater. Science and Engineering A 172, 71–78.

Weerasooriya, T., Moy, P., Dowding, R., 1994. Effect of W-W contiguity on the high shear strain rate behavior of 93W–5Ni–2Fe tungsten heavy alloy. In: Bose, A., Dowding, R. (Eds.), Proceedings of the Second International Conference on Tungsten and Refractory Metals. Metal Powder Industries, pp. 401–409.

Weibull, W., 1951. A statistical distribution function of wide applicability. J. Appl. Mech. 18, 293–297.

Yano, K., Horie, Y., 1999. Discrete-element modeling of shock compression of polycrystalline copper. Phys. Rev. B 59, 13672–13680.

Yano, K., Horie, Y., 2002. Mesomechanics of the α–β transition in iron. Int J Plasticity 18, 1427–1446.

Zhou, F., Molinari, J.-F., 2004. Stochastic fracture of ceramics under dynamic tensile loading. Int. J. Solids Struct. 41, 6573–6596.

Zhou, M., 1993. Dynamic shear localization in a tungsten heavy alloy and ductile rupture in a spheroidized 1045 steel. Ph.D. Thesis, Division of Engineering, Brown University, Providence, RI.

Zhou, M., 1998. Growth of shear bands in composite microstructures. Int. J. Plasticity 14, 733–754.

Zhou, M., Clifton, R.J., 1997. Dynamic constitutive and failure behavior of a two-phase tungsten composite. J. Appl. Mech. 64, 487–494.

Zhou, M., Clifton, R.J., Needleman, A., 1994. Finite element simulations of shear localization in plate impact. J. Mech. Phys. Solids 42, 423–458.

Zurek, A.K., Gray, G.T., 1991. Dynamic strength and strain rate effects on fracture behavior of tungsten and tungsten alloys. J. Phys. IV C 3, 631–637.

NO. OF COPIES	ORGANIZATION
1 (PDF ONLY)	DEFENSE TECHNICAL INFORMATION CTR DTIC OCA 8725 JOHN J KINGMAN RD STE 0944 FORT BELVOIR VA 22060-6218
1	US ARMY RSRCH DEV & ENGRG CMD SYSTEMS OF SYSTEMS INTEGRATION AMSRD SS T 6000 6TH ST STE 100 FORT BELVOIR VA 22060-5608
1	DIRECTOR US ARMY RESEARCH LAB IMNE ALC IMS 2800 POWDER MILL RD ADELPHI MD 20783-1197
1	DIRECTOR US ARMY RESEARCH LAB AMSRD ARL CI OK TL 2800 POWDER MILL RD ADELPHI MD 20783-1197
1	DIRECTOR US ARMY RESEARCH LAB AMSRD ARL CI OK T 2800 POWDER MILL RD ADELPHI MD 20783-1197

ABERDEEN PROVING GROUND

1	DIR USARL AMSRD ARL CI OK TP (BLDG 4600)

NO. OF COPIES	ORGANIZATION
	ABERDEEN PROVING GROUND
31	DIR USARL AMSRD ARL WM J MCCAULEY T WRIGHT AMSRD ARL WM MD B CHEESEMAN C-F YEN G GAZONAS AMSRD ARL WM TA T JONES S SCHOENFELD AMSRD ARL WM TC R COATES M FERMEN-COKER S SEGLETES AMSRD ARL WM TD S BILYK T BJERKE D CASEM J CLAYTON (10 CPS) D DANDEKAR M GREENFIELD Y HUANG B LOVE M RAFTENBERG E RAPACKI M SCHEIDLER T WEERASOORIYA

INTENTIONALLY LEFT BLANK.